

# Line-of-sight mass estimator and the masses of the Milky Way and Andromeda Galaxy

Danila Makarov <sup>1</sup>, Dmitry Makarov <sup>1</sup> , Kirill Kozyrev <sup>2,1</sup>  and Noam Libeskind <sup>3</sup> 

<sup>1</sup> Special Astrophysical Observatory, Russian Academy of Sciences, Nizhnii Arkhyz, 369167 Russia

<sup>2</sup> Kazan Federal University, Kazan, Russia

<sup>3</sup> Leibniz Institut für Astrophysik Potsdam (AIP), An der Sternwarte 16, D-14482, Potsdam, Germany

\* Correspondence: dim@sao.ru

**Abstract:** The total mass of a galaxy group, such as the Milky Way (MW) and the Andromeda Galaxy (M 31), is usually determined from the kinematics of the satellites within their virial zones. Bahcall and Tremaine (1981) proposed the  $v^2r$  estimator as an alternative to the virial theorem. We develop this approach by taking into account the three-dimensional distribution of satellites in the system to improve the reliability and accuracy of galaxy mass estimates. Applying this method to comprehensive dataset of Local Group satellites based on recent precise distance measurements, we estimate the total mass of MW of  $(7.9 \pm 2.3) \times 10^{11} M_{\odot}$  and M 31 of  $(1.55 \pm 0.34) \times 10^{12} M_{\odot}$ . The capability of the method is limited by the distance measurement accuracy, making it extremely useful for the Local Group, but challenging for more distant systems.

**Keywords:** Local Group; Andromeda Galaxy; Milky Way Galaxy; Dark matter

## 1. Introduction

Analysis of kinematics within virial zones is the main and sometimes the only available method to estimate the total mass of gravitating systems. For this purpose, various analogues of the virial theorem are used [1,2]. In the case of distant systems, only the line-of-sight velocities and the positions of galaxies in the sky are available for observation. This leads to serious uncertainties in the mass estimates. Taking into account the real three-dimensional distribution of satellites reduces the uncertainty associated with their projection onto the sky and, as a consequence, would improve the mass estimates of nearby groups.

Over the past two decades, thanks to the Hubble Space Telescope and advances in high-precision distance measuring techniques, breakthroughs have been made in exploring the structure of the nearest Universe. For example, according to the Color-Magnitude Diagram Catalog [3] of the Extragalactic Distances Database [4], at the moment, the tip of the red giant branch (TRGB) distances with a median accuracy of 3.7% have been measured for about 500 nearby galaxies on scales up to 10 Mpc. Thanks to this, we know the real three-dimensional distribution of satellites around giant Local Volume galaxies, and in particular the detailed structure of the groups around our Galaxy and the Andromeda Galaxy.

Moreover, in most cases in nearby groups the central galaxy dominates its suite in luminosity and mass. Therefore, a simple model of a point mass surrounded by test particles can be used. This is exactly the model considered in the work of Bahcall and Tremaine [1]. Thus, the aim of this work is to develop their projection mass estimator taking into account the three-dimensional distribution of satellites, and to study its applicability to nearby groups of galaxies. Since the only remaining uncertainty is the projection of the satellite velocity onto the line of sight, we call this approach the line-of-sight mass estimator.

The article is organized as follows. Section 2 briefly describes the projection mass method. Section 3 is devoted to the line-of-sight mass estimator. Its application to the mass estimation of our Galaxy and the Andromeda Galaxy is discussed in Section 4. Comparison with numerical models

and analysis of the influence of distance errors are performed in Sections 5 and 4.3, respectively. We conclude in Section 6.

## 2. Projection mass method

By considering the motion of test particles around a point mass, Bahcall and Tremaine [1] show that due to projection effects, the virial theorem estimate of the galaxy group mass,  $M_{\text{vir}}$ , is statistically:

1. *biased*, namely the average of  $M_{\text{vir}}$  estimates for the same group is not necessarily equal to the true mass for a finite number of particles;
2. *inefficient* and its variance is large;
3. *inconsistent* in some cases, that is,  $M_{\text{vir}}$  does not converge to the true mass when  $N \rightarrow \infty$ .

The main reason for the inefficiency of the virial mass is the uncertainty introduced by the projection factor in the distances between galaxies. But even ignoring projection effects,  $M_{\text{vir}}$  remains ineffective, since nearby particles contribute more than distant ones to both the estimate of kinetic energy, as the sum of squared velocities, and to the estimate of potential energy,  $\sum_i v_i^2$ , as the harmonic mean of distances,  $\sum_i 1/r_i^2$ . Since both distant and nearby particles carry the same information about the central mass, it is clear that the virial estimate  $M_{\text{vir}}$  does not effectively use all the available information.

As an alternative to the virial theorem, Bahcall and Tremaine [1] propose to use the so-called projection mass estimate, based directly on the observed values

$$GM_{\text{p}} = av_{\text{los}}^2 r_{\text{p}}, \quad (1)$$

where  $v_{\text{los}}$  is the line-of-sight velocity of the particle with respect to the central body, and  $r_{\text{p}}$  is its projected separation. This method uses equally the information about the test particles at all distances, as on average  $\langle v_{\text{los}}^2 r_{\text{p}} \rangle = \text{const}$ . The correction coefficient  $a$  is determined by averaging over all possible trajectories of particles in the system. As a result, for the typical case of observing a distant group with a dominant massive galaxy, Bahcall and Tremaine [1] obtain

$$GM_{\text{p}} = \frac{32}{\pi(3 - 2\langle e^2 \rangle)} \langle v_{\text{los}}^2 r_{\text{p}} \rangle. \quad (2)$$

To get a realistic estimate of the mass, one must make an assumption about the particle orbits. The most natural assumption is that the velocity distribution is isotropic, with eccentricity  $\langle e^2 \rangle = 1/2$ . In this case, the projected mass estimator,  $M_{\text{I}}$ , becomes

$$GM_{\text{I}} = \frac{16}{\pi} \langle v_{\text{los}}^2 r_{\text{p}} \rangle, \quad (3)$$

with the variance of

$$\text{Var}(\langle GM_{\text{I}} \rangle) = \frac{1}{N} \left( \frac{128}{5\pi^2} - 1 \right) \langle GM_{\text{I}} \rangle^2, \quad (4)$$

where  $N$  is the number of test particles.

## 3. Line-of-sight mass method

Our goal is to obtain a correction factor for the mass estimator based on an expression of the form

$$GM_{\text{Ios}} = av_{\text{los}}^2 r, \quad (5)$$

where  $v_{\text{los}}$  is the line-of-sight velocity of the test particle and  $r$  is the spatial separation with respect to the central body. Hereafter, we follow the notation and approach used in the work by Bahcall and

Tremaine [1]. The average of any quantity  $\zeta(\mathbf{r}, \mathbf{v})$  can be found by integrating over the distribution function  $f(\mathbf{r}, \mathbf{v})$  of a spherically symmetric gravitating system.

$$\langle \zeta \rangle = A \int_0^\infty r^2 dr \int_0^\pi \sin \Theta d\Theta \int_0^\infty v_\perp dv_\perp \int_{-\infty}^\infty dv_r \int_0^{2\pi} \zeta f d\phi', \quad (6)$$

where  $\Theta$  is the polar angle of the radius vector  $\mathbf{r}$  in a spherical coordinate system, where the polar axis is directed toward the observer;  $\phi'$  is the azimuthal angle of the velocity vector  $\mathbf{v}$  in a cylindrical system, where the z-axis is located along the radius vector;  $v_r$  and  $v_\perp$  are the components of the velocity vector directed along and perpendicular to the radius vector, respectively.

The distribution function of a spherically symmetric gravitating system can depend only on the energy,  $E = GM/r - v^2/2$ , and the square of the angular momentum,  $J^2 = r^2 v_\perp^2$ . Using the exact values of the energy,  $E_0$  and the angular momentum  $J_0$ , the distribution function can be expressed in terms of the Dirac delta function:

$$\begin{aligned} f &= f_0(E, J) = \delta(E - E_0) \delta(J^2 - J_0^2) \\ &= \delta(GM/r - v^2/2 - E_0) \delta(r^2 v_\perp^2 - J_0^2). \end{aligned} \quad (7)$$

Given the property of the delta function,

$$\delta(f(x)) = \sum_i \frac{\delta(x - x_i)}{|f'(x_i)|},$$

where  $x_i$  are roots of the function  $f(x)$ , the equation (6) is transformed to

$$\begin{aligned} \langle \zeta \rangle &= A \int_0^\infty r^2 dr \int_0^\pi \sin \Theta d\Theta \int_0^\infty v_\perp dv_\perp \int_{-\infty}^\infty dv_r \\ &\quad \times \int_0^{2\pi} \zeta \delta(GM/r - v^2/2 - E_0) \delta(r^2 v_\perp^2 - J_0^2) d\phi' \\ &= A \int_{r_{\min}}^{r_{\max}} r^2 dr \int_0^\pi \sin \Theta d\Theta \int_0^{2\pi} \zeta \frac{2}{|v_r|} \frac{1}{|2r^2|} d\phi' \\ &= A \int_{r_{\min}}^{r_{\max}} dr \int_0^\pi \sin \Theta d\Theta \int_0^{2\pi} \frac{\zeta}{|v_r|} d\phi' \end{aligned} \quad (8)$$

where

$$v_\perp^2 = J_0^2/r^2 = \frac{(GM)^2}{2E_0} (1 - e^2) \frac{1}{r^2} \quad (9)$$

$$\begin{aligned} v_r^2 &= 2GM/r - J_0^2/r^2 - 2E_0 \\ &= 2 \frac{GM}{r} - \frac{(GM)^2}{2E_0} (1 - e^2) \frac{1}{r^2} - 2E_0, \end{aligned} \quad (10)$$

and it is taken into account that the maximum angular momentum for a given energy  $E_0$  is  $J_{\max} = GM/(2E_0)^{1/2}$ , and the eccentricity is defined as  $e^2 = 1 - (J/J_{\max})^2$ . The integration limits are defined by the relations  $v_r(r_{\min}) = v_r(r_{\max}) = 0$  and are equal to

$$r_{\min} = \frac{GM}{2E_0} (1 - e) \quad (11)$$

$$r_{\max} = \frac{GM}{2E_0} (1 + e). \quad (12)$$

The normalization coefficient  $A$  is found from considerations of  $\langle 1 \rangle = 1$  [1]

$$A = \left( 4\pi \int_{r_{\min}}^{r_{\max}} \frac{dr}{|v_r|} \right)^{-1} = \frac{(2E_0)^{3/2}}{4\pi^2 GM}. \quad (13)$$

As noted by Bahcall and Tremaine [1], the variance of the mass estimator of the type (5) is well defined and can be determined similarly. Let us define the value

$$(GM_{\text{los}})^2 = b(v_{\text{los}}^2 r)^2. \quad (14)$$

Then the variance is

$$\begin{aligned} \text{Var}(GM_{\text{los}}) &= \text{Var}(av_{\text{los}}^2 r) = a^2 \text{Var}(v_{\text{los}}^2 r) \\ &= a^2 \left( \langle (v_{\text{los}}^2 r)^2 \rangle - \langle v_{\text{los}}^2 r \rangle^2 \right) = a^2 \left( \frac{(GM)^2}{b} - \left( \frac{GM}{a} \right)^2 \right) \\ &= \left( \frac{a^2}{b} - 1 \right) (GM_{\text{los}})^2. \end{aligned} \quad (15)$$

Accordingly, the variance of the mean  $\langle GM \rangle$  is equal to

$$\text{Var}(\langle GM_{\text{los}} \rangle) = \frac{1}{N} \left( \frac{a^2}{b} - 1 \right) \langle GM_{\text{los}} \rangle^2, \quad (16)$$

where  $N$  is the number of the test particles.

Our case of finding the average  $\langle v_{\text{los}}^2 r \rangle$  actually turns into two: when the observer sits practically in the center of the group (the case of the Milky Way) and when he views the system from the side (the case of all other nearby groups of galaxies).

### 3.1. Milky Way case

In the case of the Milky Way group, we are almost at the center of the system with respect to the distribution of satellites. As a consequence, the line of sight almost coincides with the radial coordinate, and with a good approximation we can consider  $v_{\text{los}} \approx v_r$ . Thus,

$$\langle v_{\text{los}}^2 r \rangle = \langle v_r^2 r \rangle = 4\pi A \int_{r_{\min}}^{r_{\max}} r |v_r| dr = \frac{GM}{2} \langle e^2 \rangle. \quad (17)$$

Consequently, the line-of-sight mass estimator for the Milky Way is

$$GM_{\text{los}} = \frac{2}{\langle e^2 \rangle} \langle v_r^2 r \rangle. \quad (18)$$

To estimate the variance, we obtain the value

$$\langle (v_{\text{los}}^2 r)^2 \rangle = (GM_{\text{los}})^2 \left( \frac{3}{2} e^2 - 1 + (1 - e^2)^{3/2} \right), \quad (19)$$

which gives us the variance of the mass estimate for our Galaxy equal to

$$\text{Var}(\langle GM_{\text{los}} \rangle) = \frac{1}{N} \frac{4}{\langle e^2 \rangle} \left( \frac{3}{2} \langle e^2 \rangle - 1 + (1 - \langle e^2 \rangle)^{3/2} \right). \quad (20)$$

In the case of isotropic velocity distribution  $\langle e^2 \rangle = \frac{1}{2}$ , the line-of-sight mass estimator and its variance become

$$GM_{\text{I}} = 4 \langle v_r^2 r \rangle \quad (21)$$

$$\text{Var}(\langle GM_{\text{I}} \rangle) = \frac{4(\sqrt{2} - 1)}{N} \langle GM_{\text{I}} \rangle^2 \approx \frac{1.657}{N} \langle GM_{\text{I}} \rangle^2. \quad (22)$$

### 3.2. Nearby group case

Consider the case where an observer is at a sufficient distance from the group. In addition, the three-dimensional distribution and line-of-sight velocities of the satellites are known from observations. This case corresponds to nearby groups of galaxies in the Local Volume, where high-precision distances have been measured for a large number of galaxies. Then the line-of-sight velocity can be represented as  $v_{\text{los}} = v_r \cos \Theta - v_{\perp} \sin \phi' \sin \Theta$ . The equation (8) is transformed to the form

$$\langle v_{\text{los}}^2 r \rangle = \frac{4\pi A}{3} \int_{r_{\text{min}}}^{r_{\text{max}}} r v_r \left( 1 + \frac{v_{\perp}^2}{v_r^2} \right) dr = \frac{GM}{6} (2 - \langle e^2 \rangle). \quad (23)$$

Similarly, for the mean square we obtain

$$\langle (v_{\text{los}}^2 r)^2 \rangle = \frac{(GM)^2}{10} (2 - \langle e^2 \rangle) \quad (24)$$

The corresponding mass estimator and its variance are

$$GM_{\text{los}} = \frac{6}{2 - \langle e^2 \rangle} \langle v_{\text{los}}^2 r \rangle \quad (25)$$

$$\text{Var}(\langle GM_{\text{los}} \rangle) = \frac{1}{N} \left( \frac{36}{10(2 - \langle e^2 \rangle)} - 1 \right) \langle GM \rangle^2. \quad (26)$$

For an isotropic distribution over orbits  $\langle e^2 \rangle = \frac{1}{2}$  we obtain

$$GM_{\text{I}} = 4 \langle v_{\text{los}}^2 r \rangle \quad (27)$$

$$\text{Var}(\langle GM_{\text{I}} \rangle) = \frac{7}{5N} \langle GM_{\text{I}} \rangle^2 = \frac{1.4}{N} \langle GM_{\text{I}} \rangle^2. \quad (28)$$

Note that despite the fundamental difference in the general expressions for the mass of the Milky Way (eq. 17) and the nearby group (eq. 23), the correction factors for the isotropic case in eq. (21) and (27) coincide surprisingly.

## 4. Application to the Local Group of galaxies

The Local Group of galaxies needs no special introduction. It is a fairly isolated system with a radius of about 1 Mpc. The nearest comparable galaxy groups are at a distance of 3–4 Mpc [5]. The Local Group is based on two giant spiral galaxies separated by 780 kpc, the Milky Way (MW) and the Andromeda Galaxy (M 31), which are similar to each other in many ways. These giants are surrounded by rich suites of satellites that extend up to 300 kpc. Only about a dozen dwarf galaxies are known in the Local Group outside the virial zones of MW and M 31. Thanks to modern deep optical surveys and systematic searches, our knowledge of the Local Group population has expanded dramatically. The list of satellites is growing with new members all the time. This allows one to trace their population to extremely low luminosity, which is technically inaccessible for more distant galaxy groups. The recently discovered galaxy Ursa Major III [6] has a luminosity of  $M_V = +2.2$  mag, corresponding to a stellar mass of only  $16 M_{\odot}$ . The subsystems of the MW and M 31 satellites do not overlap, allowing them to be studied independently, without considering complex interactions. Various methods and subsystems are used to estimate the mass, from the motion of stars and gas in the galaxies themselves, to the study of the kinematics of globular clusters and satellites, the timing argument for the orbiting of MW and M 31, and the Hubble flow braking at the Local Group boundary [see recent reviews by 7–9]. All this allows us to trace the distribution of luminous and dark matter in the Local Group on a scale from units of kiloparsecs to about one megaparsec. There is a consensus that M 31 is a slightly more massive galaxy than MW [10–12], but the mass estimates for both galaxies vary widely, sometimes leading to the opposite conclusion [13]. New mass estimates for MW and M 31 remain an important goal in the study of these galaxies and the Local Group as a whole.

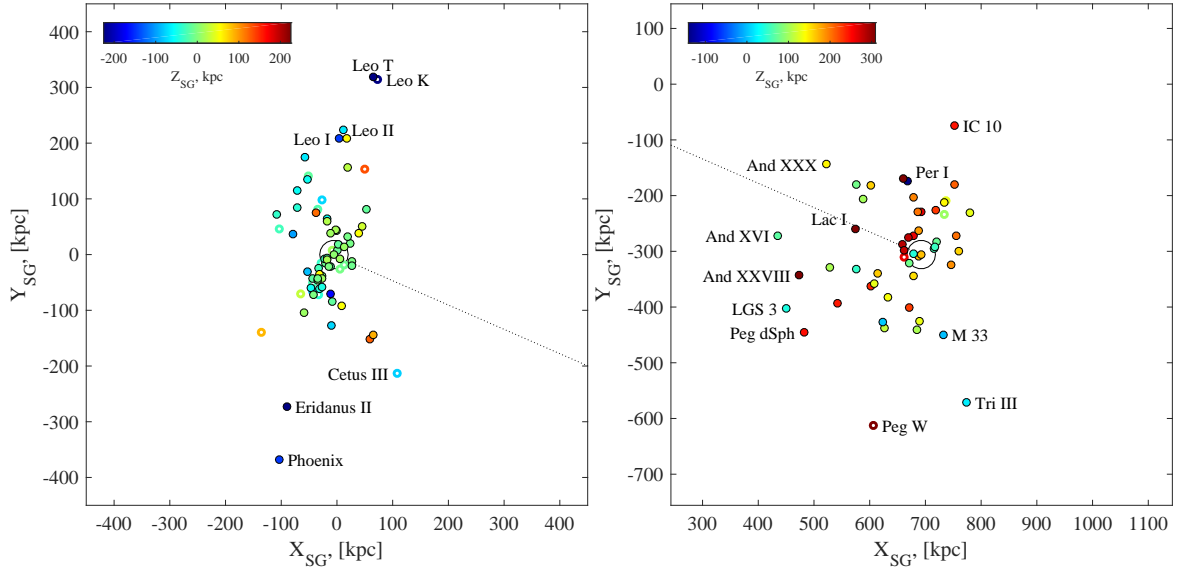


**Figure 1.** 3D-distribution of galaxies within 450 kpc from MW (left panel) and M 31 (right panel) in Cartesian Supergalactic coordinates. The Z-axis is indicated by color. Galaxies with unknown line-of-sight velocity are shown by open colored circles. The dotted line connects MW and M 31. Satellites located further than 220 kpc from the central galaxy are labeled.

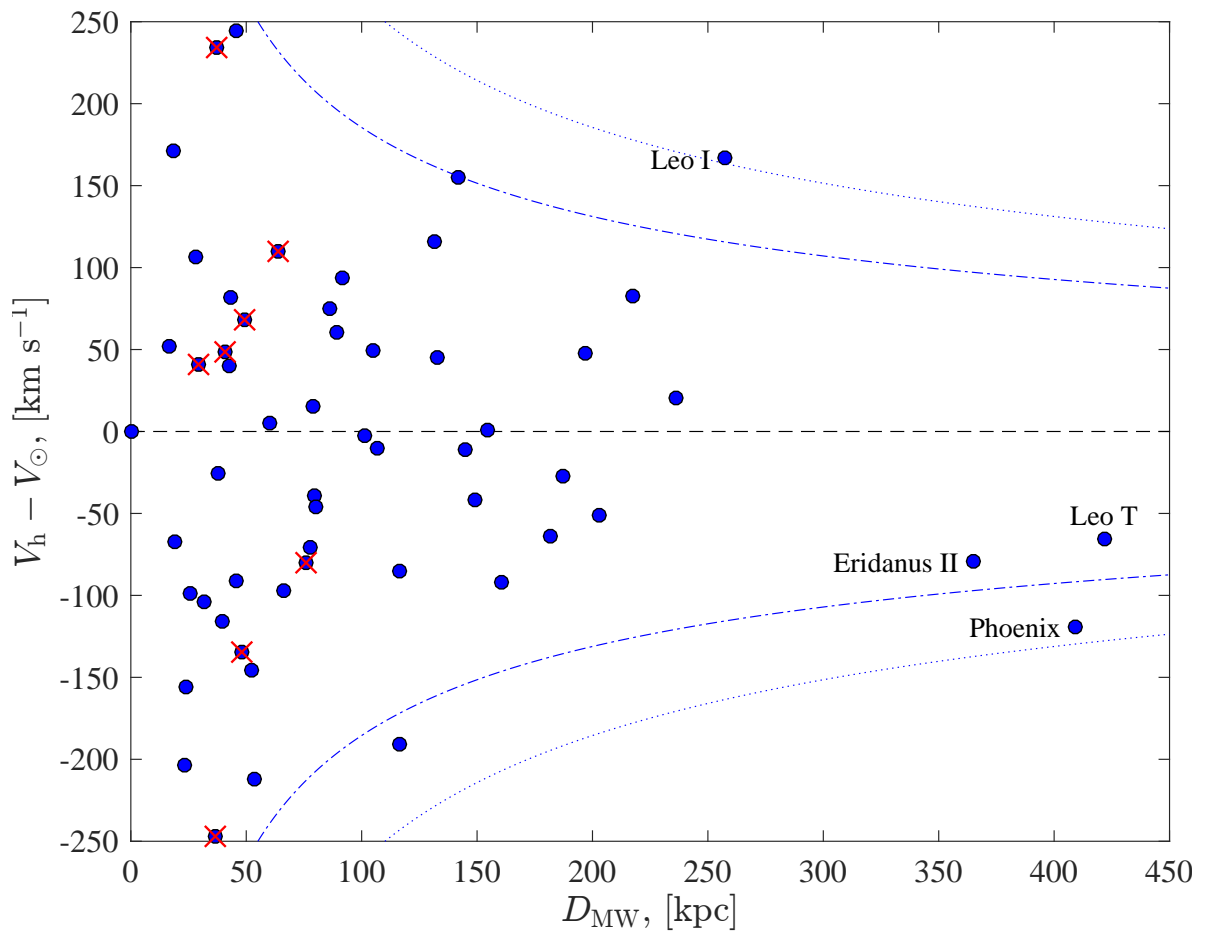
The sample of MW and M 31 satellites was gathered based on the latest version of the Local Volume galaxy database [14], taking into account recent work on studying cosmic flows around nearby massive galaxies [15], measuring proper motions of MW satellites [16,17], estimating distances from RR Lyrae variables [18], recent galaxy discoveries [for instance 19], HyperLeda [20] and NED databases, and many other works. Members of the MW and M 31 groups with compiled distances and heliocentric line-of-sight velocities are presented in Appendices A and B, respectively.

Figure 1 shows the three-dimensional distribution of satellites of our Galaxy (left panel) and the Andromeda Galaxy (right panel) in Supergalactic coordinates (the Z coordinate is indicated by color). The famous satellite planes are clearly visible around both galaxies [21]. Also, the M 31 satellites demonstrate a well-known skew toward our Galaxy [22].

#### 4.1. Milky Way

Thanks to the Gaia mission [23], the proper motions of most of the satellites of our Galaxy have been measured, which unambiguously allows us to determine all six components of the satellite position in phase space. This information is actively used to refine the structure of our Galaxy, to estimate its total mass, and to analyze the features of satellite orbits. It should be emphasized that the line-of-sight velocities of satellites are measured an order of magnitude more accurately than their proper motions. Therefore, an independent mass estimate based on simple line-of-sight velocities remains extremely important.

Moreover, even a simple analysis of the radial velocity distribution can reveal unexpected and interesting effects. Recently, Makarov et al. [24] discovered that the dipole component of the radial velocity field shows an unexpectedly large amplitude of  $226 \pm 50 \text{ km s}^{-1}$  of the bulk motion of nearby satellites at distances less than 100 kpc. This anomaly is caused by only eight galaxies (crossed out with red crosses in the left panel of Fig. 2), which include the Large Magellanic Cloud (LMC) and three galaxies from its escort. Numerical simulations demonstrate that this velocity pattern is consistent with the assumption of the first flyby of the massive LMC around our Galaxy and the perturbation it creates in the motion of the MW satellites. This example shows the importance of a careful selection of “the test particles” for kinematic analysis. Objects on the first flyby do not have time to virialize and therefore should be excluded from consideration when estimating the total mass of the system.



**Figure 2.** The velocity-distance distribution of the nearest galaxies relative to the center of our Galaxy. The circular and escape velocities of the point mass  $8 \times 10^{11} M_{\odot}$  are shown by the dashed and dotted lines, respectively.

**Table 1.** Summary of the MW mass estimates.

Sample	range [kpc]	#	$M_I$ [ $\times 10^{11} M_\odot$ ]
all	23–257	49	$8.1 \pm 1.5$
w/o Leo I	23–236	48	$6.9 \pm 1.3$
w/o 8	23–257	41	$8.1 \pm 1.6$
w/o 8 & Leo I	23–236	40	$6.7 \pm 1.4$
$D < 86$ kpc	23–86	28	$6.2 \pm 1.5$
w/o 8	23–86	20	$5.5 \pm 1.6$
$D > 86$ kpc	89–257	21	$10.7 \pm 3.0$
w/o Leo I	89–236	20	$7.9 \pm 2.3$

At present, there are 67 known satellites of our Galaxy within the 260 kpc region. As can be seen in Fig. 2, there is a clear separation between the well-randomized MW satellites up to distances of 260 kpc, indicating the extension of the virial zone, and three galaxies with systematic negative velocity at a distance of 400 kpc, which are probably just entering the MW halo for the first time. Thus, we limited the analysis area to a distance of 260 kpc.

As shown by Makarov et al. [24], after excluding eight objects that most strongly distort the behavior of the solar apex, the observed collective motion of the remaining satellites is consistent within errors with the motion of the Sun in our Galaxy. Thus, in further analysis, the observed line-of-sight velocities were simply corrected for the solar velocity vector of  $(9.5, 250.7, 8.56)$  km s<sup>-1</sup> [25] with respect to the Galactic center, determined from the proper motion of Sgr A\* of  $(-6.411 \pm 0.008, -0.219 \pm 0.007)$  mas yr<sup>-1</sup> in Galactic coordinates [26] and the distance of  $8249 \pm 9 \pm 45$  pc to the central supermassive black hole [27].

The case of Leo I deserves special attention. As can be seen in Fig. 2, this most distant satellite at the edge of the virial zone has an extremely high radial velocity. The inclusion of Leo I (just one galaxy) in the analysis leads to a dramatic 33% increase of the total MW mass [11]. Currently, it is not entirely clear whether the orbit of Leo I is elliptic or hyperbolic [28]. Nevertheless, proper motion measurements indicate that Leo I is likely bound to the Milky Way [29], but it is on an extremely elongated orbit with an eccentricity of  $0.79^{+0.10}_{-0.09}$  [17]. Nevertheless, we prefer to exclude it from the analysis, since it is drastically outliers from the general behavior of the satellites. Its orbit also obviously does not satisfy the isotropy condition that we use in the following analysis. Moreover, there is evidence of tidal stripping in this galaxy [30], indicating its violent prehistory, and as a consequence, it cannot be considered as a simple test particle.

Based on the results obtained in Section 3.1 and assuming an isotropic distribution of satellite orbits, we estimate the MW mass using different subsamples of satellites. Figure 3 presents the behavior of the running line-of-sight mass estimated from 20 satellite sequences for the case of all galaxies (dashed line) and after excluding the eight members of the group with a large collective motion (solid blue line). As you can see, the exclusion of these eight galaxies does not radically change the mass estimates, but the trend of mass growth with distance appears more clearly. This behavior is a natural consequence of the density distribution in the dark matter halos surrounding galaxies. However, due to the small statistics, errors and random fluctuations turn out to be quite large.

The results are summarized in Table 1. It gives the range of galactocentric distances of satellites, the sample size, and the corresponding mass estimate,  $M_I$ , assuming isotropic orbits. The distance of 86 kpc is chosen on the basis that at large distances the motion of the satellites is well randomized and does not show significant collective motions relative to the Galactic center [24], and this boundary also divides the sample of satellites into equal parts. It is evident that Leo I gives a significant increase in the total mass of the Galaxy, which is especially noticeable in the case of external satellites, where its contribution increases the mass estimate by 35%.

Based on this analysis, we estimate the mass of the Galaxy within 86 kpc to be in the range  $[5.5\text{--}6.2] \times 10^{11} M_\odot$  with uncertainty of  $\pm 1.5 \times 10^{11} M_\odot$ , and the total mass within 240 kpc to be



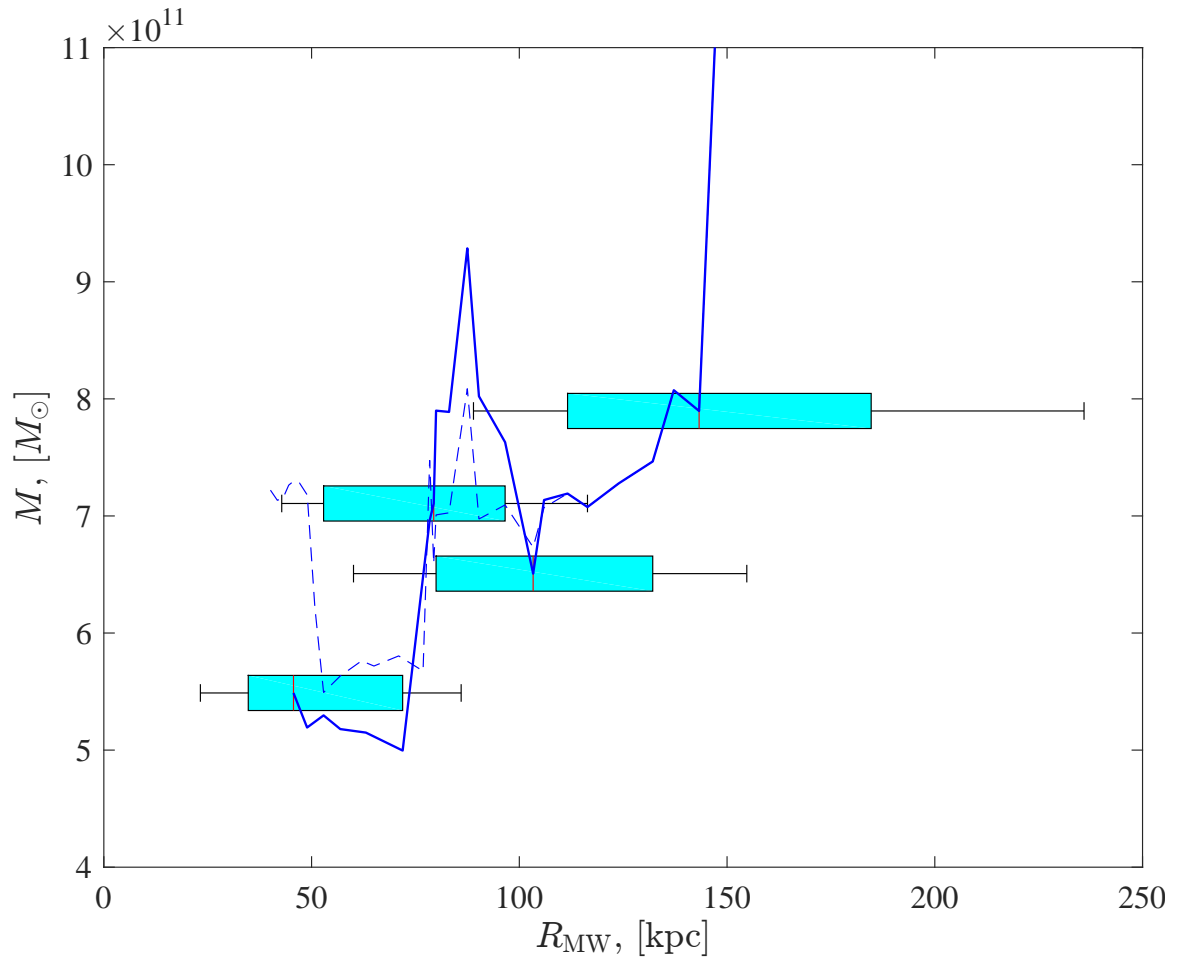


**Figure 3.** MW mass estimated from different subsamples of satellites. The box plots indicate the range, interquartile range and median for four subsamples of 20 satellites and corresponding mass estimates. The solid blue line corresponds to the running mass estimated from subsamples of 20 satellites, after excluding eight galaxies. The dashed line is the running mass for whole sample.

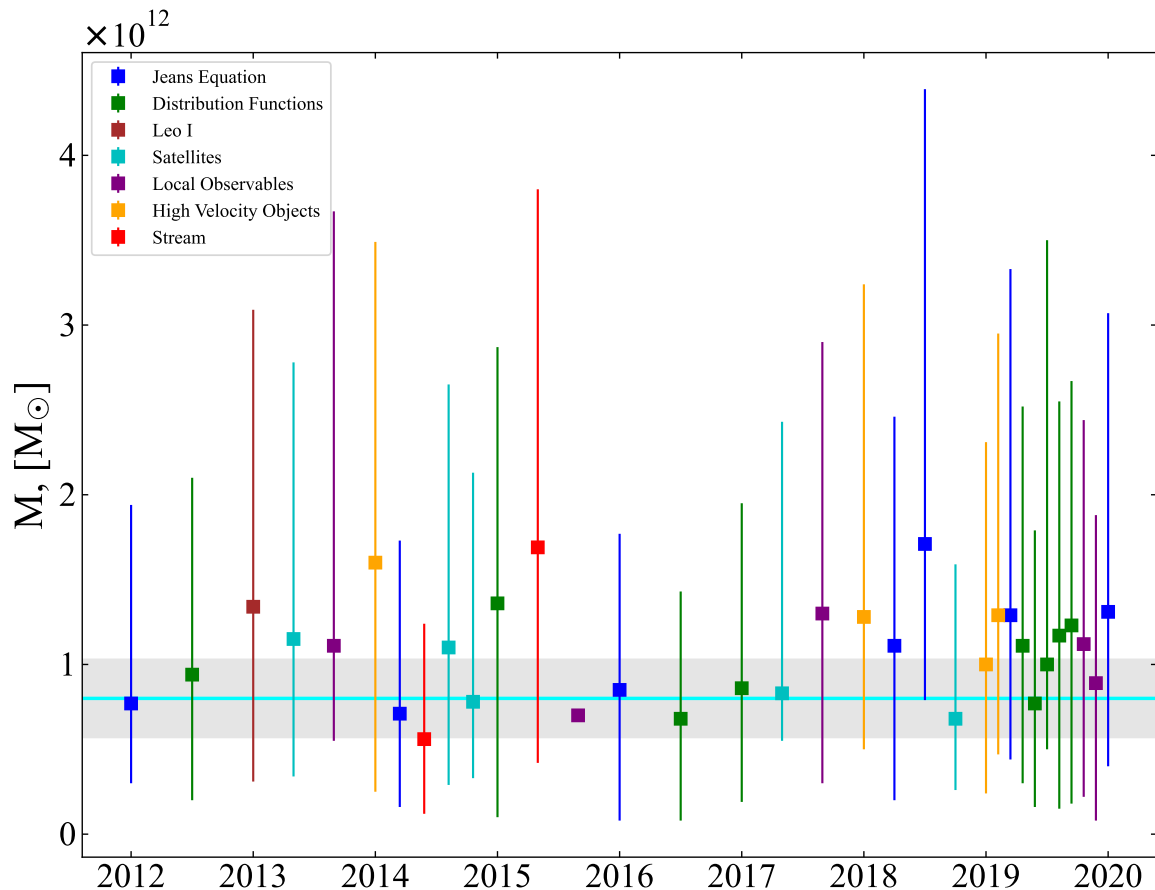


**Figure 4.** Comparison of our estimate of the MW mass with recent measurements obtained by different authors.

$(7.9 \pm 2.3) \times 10^{11} M_{\odot}$ . The latter value is in good agreement with numerous estimates by other authors [see Fig. 4 based on recent reviews by 7,8].

#### 4.2. Andromeda Galaxy

The sky distribution of the 55 known neighbors of M 31 within 525 kpc of it is shown in Fig. 5. Unlike the MW satellites, the proper motions in the Andromeda group are known only for a few galaxies: M 31 [31,32], M 33 [31,33], NGC 185, NGC 147, IC 10 [33] and And III [34]. However, the tangential velocity is determined with large errors and the significance of such measurements rarely exceeds 4 sigma. Therefore, to estimate the M 31 mass from the satellite motions, we must still rely only on their line-of-sight velocities.

The transverse velocity of the Andromeda Galaxy relative to our Galaxy also remains highly controversial [see fig. 6 in 32]. Salomon et al. [32] conclude that the approach of these two giant galaxies is radial. Correction of the observed velocity of M 31 for the solar motion in the Galaxy gives the approach velocity equal to  $-109 \text{ km s}^{-1}$ . Unfortunately, the fairly compact location of the M 31 satellites in the sky leaves no chance to estimate the tangential velocity of the system using only line-of-sight velocities. We can only test the velocity component toward M 31. The average line-of-sight velocity of the M 31 satellite system within 200 kpc is  $-105 \pm 20 \text{ km s}^{-1}$ , which is almost identical to the velocity of the central galaxy. Beyond 200 kpc, the average velocity of the satellites diverges from that of M 31, reaching  $\Delta V \approx 35 \text{ km s}^{-1}$ , under the influence of M 33, its satellites And XXII and Tri III, and NGC 185. Therefore, for further analysis, we assume a head-on approach of our Galaxy and the Andromeda Galaxy with  $V = -109 \text{ km s}^{-1}$ .

We estimate the total mass of the Andromeda Galaxy using the line-of-sight mass estimator assuming isotropy of the orbits for the case of observing the system from the outside (Section 3.2). The results for different satellite subsamples are summarized in Table 2. In addition to the sample size (#), the velocity dispersion ( $\sigma_V$ ), and the line-of-sight mass ( $M_l$ ), it also provides the line-of-sight mass

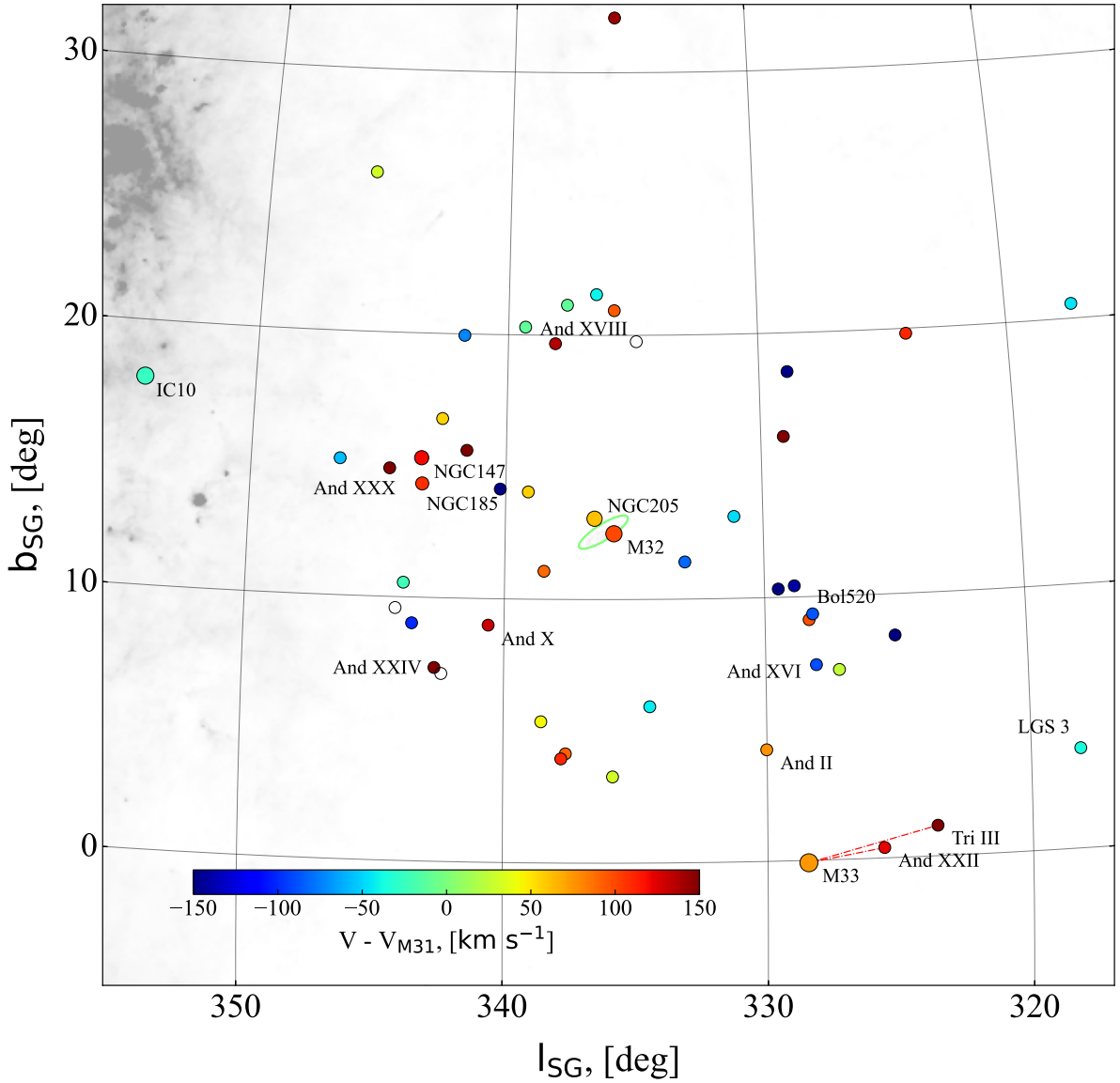


**Figure 5.** Distribution of the M 31 satellites in the sky in the Aitoff projection. M 31 is shown by a central ellipse. The color reflects the velocity difference relative to the central galaxy. The open dots mark galaxies with unknown line-of-sight velocities. The IRAS interstellar extinction map is given by gray clouds.

**Table 2.** Summary of the M 31 mass estimates.

Sample	#	$\sigma_V$ $\text{km s}^{-1}$	$M_I$		
			$M_I$	$M_I^c$	$M_I^p$
			$\times 10^{11} M_\odot$		
<i>cz</i>	38	117.5			$17.4 \pm 4.4$
<i>D &amp; cz</i>	33	114.1	$18.5 \pm 3.8$	$16.9 \pm 3.5$	$21.7 \pm 6.0$
w/o 2 <sup>†</sup>	31	113.6	$18.5 \pm 3.9$	$16.9 \pm 3.6$	$19.5 \pm 5.5$
w/o 3 <sup>‡</sup>	30	112.7	$17.0 \pm 3.7$	$15.5 \pm 3.4$	$17.4 \pm 5.0$

<sup>†</sup> excluding M 33 subgroup

<sup>‡</sup> excluding M 33 subgroup and And XXX

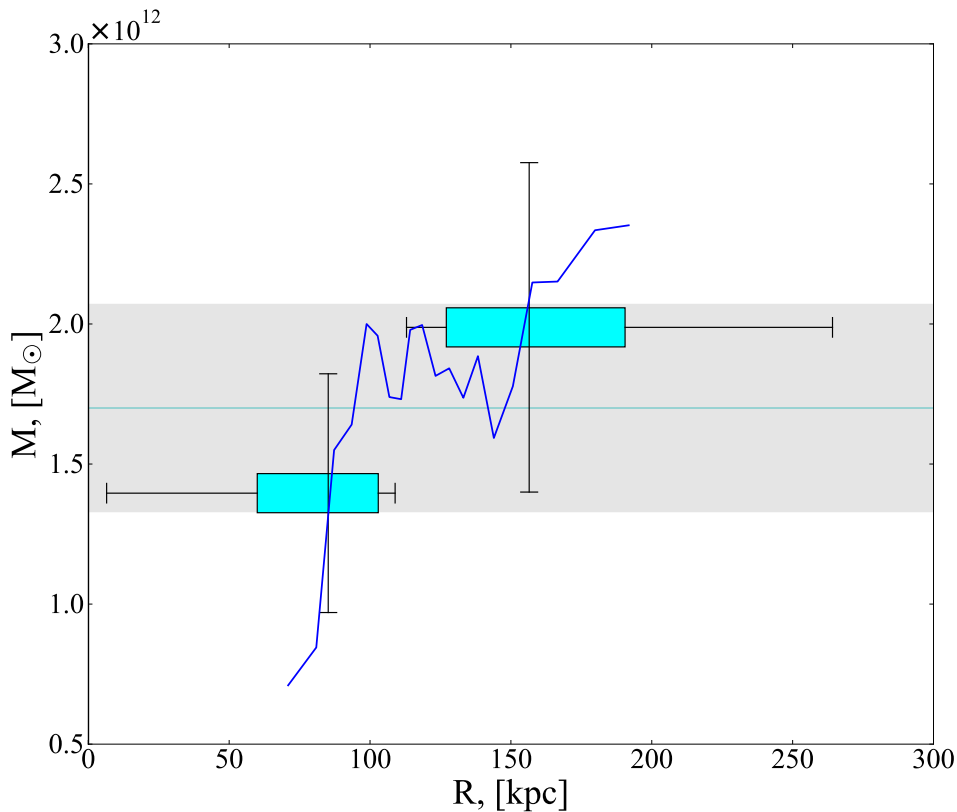


**Figure 6.** Resulted mass estimate of the Andromeda Galaxy as a function of distance. Two boxes correspond with both near and distant subsamples, each containing 15 satellites. Boxes indicate the distance ranges and medians and mass uncertainty. General mass estimate  $M = (1.70 \pm 0.37) \times 10^{12} M_{\odot}$  (cyan line) with its error (gray filling) is provided. The solid blue line reflects shifts in dynamics of the running mass for the entire sample.

( $M_1^c$ ) corrected for the distance errors (see Section 4.3), and the mass obtained by the classical projected mass method ( $M_1^p$ ) proposed by Bahcall and Tremaine [1]. The description of the subsamples is given below.

As in the case of our Galaxy, the sample of M 31 satellites for mass determination requires some careful consideration. From the total list of 48 satellites around the Andromeda Galaxy within 300 kpc, we excluded all objects with unknown, questionable, or imprecise distance measurements, because they could be a source of large systematic errors. Among them are 11 objects from the Pan-Andromeda Archaeological Survey (PAndAS) without distance measurements. We also excluded all objects, whose distance errors are greater than 5%, namely: Tri III (6.4%), probably satellite of M 33 [35]; a globular cluster Bol 520 (9.6%); IC 10 (5.7%) and And XXVII (5.7%), which reside in the region of high MW extinction. This sample is designated as ‘*D & cz*’ in Table 2.

The Andromeda group has its own LMC analog. As shown by Patel et al. [36], M 33 is located near the apocenter of its first flyby around the Andromeda Galaxy. A plume of neutral hydrogen stretches along its trajectory. Therefore, we excluded from consideration M 33 with its suit of And XXII and Tri III<sup>1</sup> as unsatisfying the requirement of isotropy of their orbits and virialization in the system. This sample is labeled as ‘*w/o 2*’ because it excludes 2 galaxies. For a similar reason, we do not include in consideration And XVIII at a distance of  $1.33^{+0.06}_{-0.09}$  Mpc [37], which is located beyond the Andromeda Galaxy at a distance of 579 kpc and has not yet reached its virial zone. And XXX has an extremely high radial velocity  $V = 159.6 \text{ km s}^{-1}$  relative to Andromeda, so in addition to the M 33 subgroup, we also excluded it from the analysis, as it could significantly distort the data. We call the sample ‘*w/o 3*’.

We believe that the latter sample provides the most realistic estimate of the mass. Thus, our final sample contains 30 satellites within 300 kpc of M 31. Their distribution is characterized by the standard

<sup>1</sup> Tri III has already been excluded in the previous step due to insufficient distance measurement accuracy.

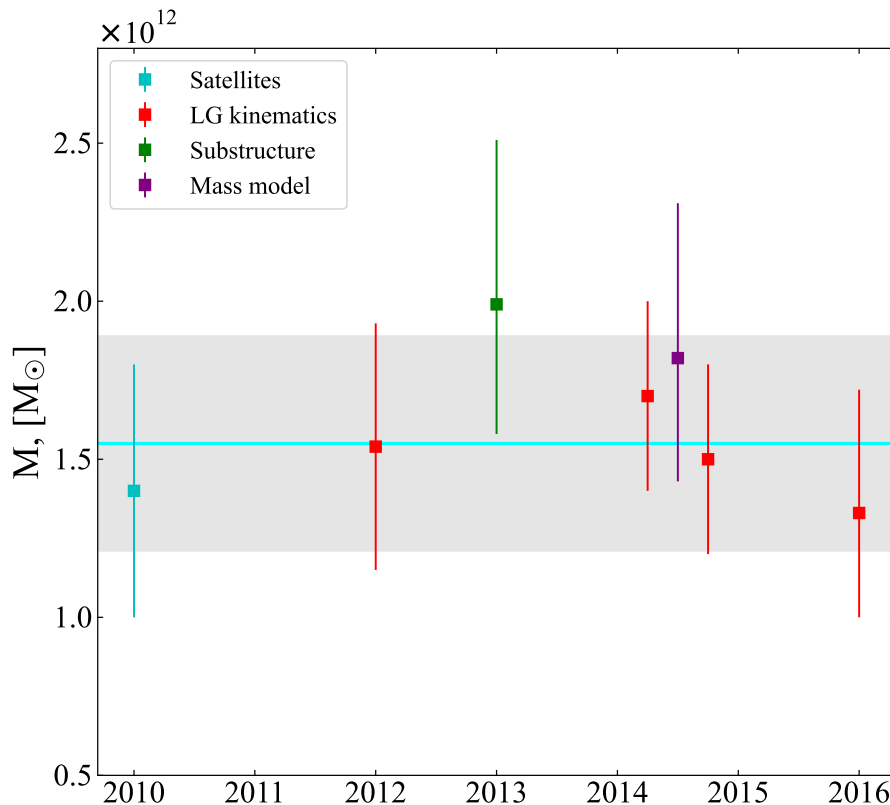


**Figure 7.** Comparison of our M 31 mass estimate (cyan line) with recently published mass estimates on the scale of 300 kpc using different methods.

deviation of the line-of-sight velocity  $\sigma_V = 112.7 \text{ km s}^{-1}$  and the average distance of  $\langle r \rangle = 138 \text{ kpc}$  from the Andromeda Galaxy. Using the line-of-sight velocity method for nearby groups (Section 3.2), we estimate the total mass of M 31 equal to  $M_I = (1.70 \pm 0.37) \times 10^{12} M_{\odot}$ . As in the case of our Galaxy, the running mass and subsamples of nearby and more distant satellites show a trend in mass on the scale from 100 to 200–300 kpc (Fig. 6).

It would be useful to compare this result with the classical approach based on the use of projected distances and radial velocities only. Using the same list of satellites, the projected mass method [1] gives a very close mass estimate of  $M_I^p = (1.74 \pm 0.50) \times 10^{12} M_{\odot}$ , but with worse accuracy. However, it also allows us to include objects in the analysis without precise distance measurements and improve accuracy through statistics. Using the 38 confirmed satellites and candidates within projected radius of 300 kpc of the Andromeda Galaxy (the sample ‘cz’), we obtain a mass of  $M_I^p = (1.74 \pm 0.44) \times 10^{12} M_{\odot}$ . It can be seen that the accuracy is still lower than in our approach. This indicates the importance of knowing the distribution of satellites in space for a more accurate estimate of the galaxy mass.

#### 4.3. Influence of the distance measurement errors

The previous result was obtained under the assumption that we know the galaxy distances absolutely precisely. Unfortunately, random errors in distance measurements lead to a systematic bias in the measured average separation of the satellites from the central galaxy and to a fictitious stretching of the system along the line of sight. As a result, we will overestimate the value of  $v^2 r$  and as a consequence the mass of the galaxy group. This effect can be especially significant when distance errors become comparable to the characteristic size of the system.

The typical accuracy of distance measurements in the near Universe is 3–4%. For the satellites of our Galaxy, this corresponds to a typical distance error of the order of a few kpc, which is negligible compared to the virial radius of the Milky Way. In the case of the Andromeda Galaxy, the situation is worse. At the distance of M 31, the typical error is 20–30 kpc, which is on the order of 10% of its virial radius.

To estimate the contribution of this systematic uncertainty to the mass of M 31, we apply the Monte Carlo method, which allows us to simulate distance measurements and the propagation of errors in a controlled manner. Assuming a Gaussian distribution of distance modulus errors, we randomly vary the measured distance modulus according to its measurement accuracy for all galaxies in the group including M 31 itself. The resulting moduli are then converted into linear distances in the standard way. All this leads to an asymmetric shift of galaxies along the line of sight relative to their original position. The mass estimate is made using exactly the same procedure as for the real galaxy group. Based on 100,000 random generations, we find that the observed distance errors lead to an effective overestimation of the mass by 9.7% with a standard deviation of 3%. As a result, for our final sample of 30 satellites, we obtain a corrected M 31 mass of  $M_1^c = (1.55 \pm 0.34) \times 10^{12} M_\odot$ , where the error takes into account the small spread introduced by distance measurement errors. As can be seen in Fig. 7 based on a review by Bhattacharya [9], this value is in excellent agreement with 7 recent estimates of the M 31 mass on the scale of 300 kpc, the average of which is  $(1.61 \pm 0.09) \times 10^{12} M_\odot$  with the standard deviation of  $0.24 \times 10^{12} M_\odot$ .

## 5. Comparison with cosmological simulations

To check the applicability of the method, we tested it using the High-resolution Environmental Simulations of The Immediate Area [HESTIA, 38]. It is a set of cosmological models designed to simulate the Local Group of galaxies. These constrained dark-matter and Magneto-Hydrodynamic simulations are based on the AREPO code [39]. The initial conditions are chosen from the peculiar velocities of the CosmicFlows-2 survey of nearby galaxies [40] using a reverse Zeldovich approximation [41]. Baryonic physics follows the AURIGA galaxy formation model [42].

The simulations include a high-resolution region of 3–5 Mpc around the Local Group analog, where galaxies similar to the Milky Way and Andromeda Galaxy are formed. In this area, a mass resolution of  $m_{\text{dm}} = 1.2 \times 10^6$  and a gas particle resolution of  $m_{\text{gas}} = 1.8 \times 10^5 M_\odot$  are achieved. These simulated galaxies match observations in terms of various physical and morphological properties, making them useful for studying the role of the surrounding environment in galaxy evolution [38]. Thanks to the technique of constrained simulations, the Local Group analog appears to be surrounded by structures that reproduce real-life environments: Virgo-like cluster, local void, local sheet, etc.

HESTIA provides three high-resolution models of the Local Group. We are primarily interested in the positions of the halos in space and their peculiar velocity vectors at  $z = 0$ . All relevant quantities are expressed in simulation units and can be rescaled to different cosmological parameters if needed. We focus on region within 200 kpc (which is closely equal to 300 kpc if  $H_0 = 67.8 \text{ km s}^{-1} \text{ Mpc}^{-1}$ ) around the two most massive halos, the MW and M 31 analogs, and mimic real observations. Namely, we place an observer in the center of the massive halo and determine, on the basis of positions and peculiar velocities, the observed line-of-sight velocities of all surrounding halos. As a result, we obtain two sets of data for the case of observing the satellites of given halo and for the case of observing satellites in a next massive halo. In total, we get six datasets for each case. In our tests, we apply the line-of-sight mass estimator assuming isotropic orbits (Section 3) to three samples: ‘satellites’ whose halos contain star particles with stellar mass  $m_* > 1.5 \times 10^5 M_\odot$ ; for massive halos  $m_{\text{dm}} > 4.3 \times 10^7 M_\odot$ ; and for all halos.

Figure 8 illustrates the case of the second most massive halo, the analog of MW, in the 17\_11 HESTIA run. Its total mass is  $M_{\text{tot}} = 1.33 \times 10^{12} M_\odot$ , while the largest halo, the analog of M 31, has  $M_{\text{tot}} = 1.56 \times 10^{12} M_\odot$ . The top panel shows the radial velocity of surrounding halos as a function of distance, while the other two panels show the mass estimates as a function of distance from the halo. The middle panel corresponds to the observation from the center of this halo, and the right panel reflects the observations of the system from the center of the neighboring most massive halo. The first thing to note is the significant difference in the velocity-distance distribution of satellites (top panel of Fig. 8) compared to that observed around the Milky Way (Fig. 2). The HESTIA ‘satellites’ (the halos with stars) within 50 kpc in the 17\_11 run have very low line-of-sight dispersion  $\sigma_V = 36.3 \text{ km s}^{-1}$

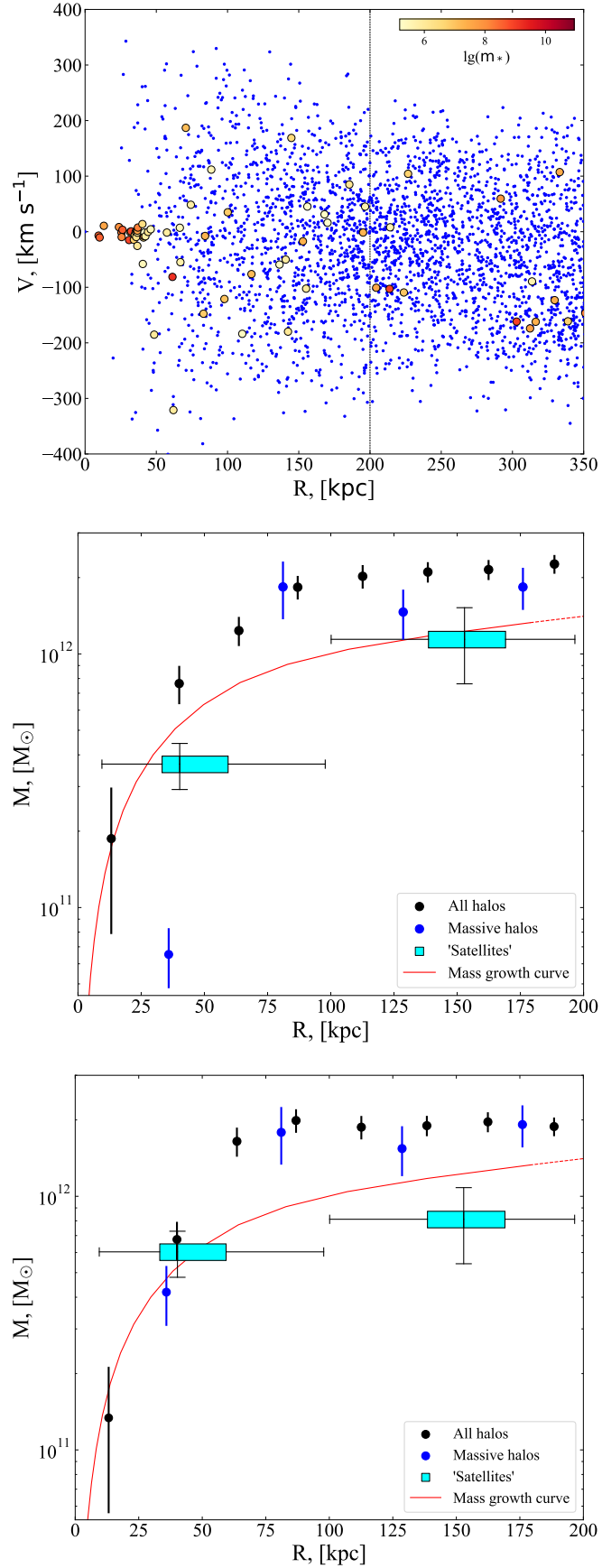


**Figure 8.** *Top panel:* The Hubble diagram for all simulated particles around the massive halo. Small blue dots represent the distribution of all dark matter halos. Satellite-like halos with  $m_* > 1.5 \times 10^5 M_\odot$  are shown by big color dots. *Middle panel:* Mass estimates for the case of observation from inside the massive halo. The cyan boxes show mass estimates for two subgroups of ‘satellites’ (54 halos in total), each spanning 100 kpc. In addition, the 8 black dots with error bars show mass estimates obtained from all 1296 halos split into 25 kpc regions, while the 4 blue dots are estimates for 139 massive halos with  $m_{\text{dm}} > 4.3 \times 10^7 M_\odot$  divided into 50 kpc regions. The solid red line depicts the cumulative mass profile  $M(< r)$  of the halo. *Bottom panel:* Similar to the previous graph, but for the case of observation from another massive halo.

compared to  $\sigma_V = 113.3 \text{ km s}^{-1}$  for more distant halos. This reflects the effects of dynamic friction and the reorganization of the orbits of the nearest halos into more circular ones, as well as the impact of the smaller mass enclosed within this radius. In addition, in this zone, there are significant selection effects of the halo identification, which is reflected in the halo deficiency at short distances from the central body. This leads to fewer statistics and, more importantly, a significant underestimate of the mass inside 50 kpc in the case of observation from the center of the system. It is important to note that the masses found for samples at different distances follow the halo mass growth curve in the simulations. The masses derived from the ‘satellites’ align well with the mass profile (median and mean of 6 simulations coincide within errors), while estimates based on all halos tend to overestimate the total mass by about 30% (significance at the 4–5 sigma level). This discrepancy may reflect the fact that the orbits of the entire halo population differ from our assumption about its isotropy.

## 6. Discussion and conclusion

We have developed a method for the mass estimation of groups with a dominant central galaxy, based on the  $v^2r$  estimator proposed by Bahcall and Tremaine [1], for the case of a known three-dimensional distribution of satellites in the system. This situation is realized in the nearby Universe, where high-precision distances for a large number of galaxies are available. Since the only unaccounted uncertainty in this case is related to the projection of the three-dimensional velocity onto the line of sight, we call this approach the line-of-sight mass estimator. As with the original projected-mass methodology, this approach requires an assumption about the nature of the satellite orbits in the system, which is expressed in terms of the mean square of the eccentricity  $\langle e^2 \rangle$ . We considered two cases: observations from the central galaxy (the case of the Milky Way and its satellites) and observations from outside the system. Despite the significant difference in the observation conditions, which is reflected in equations (17) and (23), in the case of isotropic orbits,  $\langle e^2 \rangle = 1/2$ , the correction factor for both cases turned out to be the same and equal to 4 (equations (21) and (27)). This coefficient differs from the naively expected correction of 3 for the case of a random projection of the velocity vector.

Comparison with numerical cosmological simulations confirmed the applicability of the method and showed good agreement with the true mass of the systems under the assumption of the isotropic distribution of satellite orbits. In addition, this methodology allows us to trace the distribution of the mass of the system with distance.

Unfortunately, measurement errors in distance can lead to significant bias in the mass estimate. Since the distance errors increase with distance, the applicability of the method outside the Local Group is severely limited and requires a more sophisticated Bayesian approach and a joint consideration of the assumed distribution of satellites and their velocities to obtain more reliable determination.

Application of this methodology to the Local Group allowed us to estimate the masses of the Milky Way and the Andromeda Galaxy assuming an isotropic distribution of satellite orbits.

We estimate the total mass of our Galaxy on a scale of 240 kpc of  $M_{\text{MW}} = (7.9 \pm 2.3) \times 10^{11} M_{\odot}$ . This value is in good agreement with recent measurements by other authors. Bland-Hawthorn and Gerhard [43], in their review “The Galaxy in Context”, obtained an average of individual mass estimates equal to  $(11 \pm 3) \times 10^{11} M_{\odot}$ . The average of the 33 measurements compiled by Wang et al. [7] gives the Milky Way mass on a scale of 200 kpc equal to  $M_{\text{MW}} = (10.7 \pm 0.5) \times 10^{11} M_{\odot}$  with a standard deviation of  $3 \times 10^{11} M_{\odot}$ . Bobylev and Baykova [8], based on a compilation of 20 measurements from the literature, notes that Galaxy mass estimates inside 200 kpc lie in the range  $[4\text{--}16] \times 10^{11} M_{\odot}$  with a mean of  $(8.8 \pm 0.6) \times 10^{11} M_{\odot}$  and a standard deviation of  $2.4 \times 10^{11} M_{\odot}$ .

A significantly larger mass of our Galaxy of  $(10.7 \pm 3.0) \times 10^{11} M_{\odot}$  is obtained when Leo I is included in the consideration. Its contribution outweighs all other satellites and increases the total mass by 35%. Measurements of its proper motion [17,29] indicate that Leo I is in an extremely elongated orbit with an eccentricity of  $\sim 0.8$ . Taking this effect into account should slightly reduce the contribution of Leo I compared to the other satellites, but in any case the impact remains significant. Thus, improving



the accuracy of 3D velocity measurements and clarifying the orbital parameters of Leo I is extremely important for understanding the halo structure of our Galaxy and estimating its total mass.

We estimate the total mass of M 31 of  $M = (15.5 \pm 3.4) \times 10^{11} M_{\odot}$  within a radius of 300 kpc. This value is also in excellent agreement with recent measurements. Bhattacharya [9] traced the evolution of the Andromeda Galaxy mass measurements by various methods over the last 80 years. He concluded that the average of the most accurate and reliable measurements of the last 20 years gives the M 31 mass of  $\sim 15.6 \times 10^{11} M_{\odot}$ .

Thus, measurement of the total mass of the two main galaxies of the Local Group by their satellite kinematics indicates that the M 31 is twice as massive as MW,  $M_{M31}/M_{MW} = 2.0 \pm 0.7$ . The similar ratio of  $M_{M31}/M_{MW} = 1.75^{+0.54}_{-0.28}$  is obtained by Carlesi et al. [12] using a supervised machine learning algorithm on cosmological simulation within the standard  $\Lambda$ CDM model and applying it to the distance and velocity distribution of the MW and M 31 satellites. However, it should be noted that the Hubble flow outside the virial radii of MW and M 31 indicates that the Local Group barycenter is located approximately midway between these galaxies. Karachentsev et al. [10] estimated the MW to M 31 mass ratio of  $M_{M31}/M_{MW} \simeq 4/5$ . Unfortunately, the errors in determining the masses remain large enough to speak of a statistically significant difference between these values.

**Funding:** This work was supported by the Russian Science Foundation grant № 24–12–00277

**Acknowledgments:** We acknowledge the usage of the HyperLeda database<sup>2</sup> [20]. This research has made use of the NASA/IPAC Extragalactic Database (NED), which is funded by the National Aeronautics and Space Administration and operated by the California Institute of Technology. This research has made use of the Astrophysics Data System, funded by NASA under Cooperative Agreement 80NSSC21M00561.

## References

1. Bahcall, J.N.; Tremaine, S. Methods for determining the masses of spherical systems. I. Test particles around a point mass. *ApJ* **1981**, *244*, 805–819. <https://doi.org/10.1086/158756>.
2. Heisler, J.; Tremaine, S.; Bahcall, J.N. Estimating the masses of galaxy groups: alternatives to the virial theorem. *ApJ* **1985**, *298*, 8–17. <https://doi.org/10.1086/163584>.
3. Anand, G.S.; Rizzi, L.; Tully, R.B.; Shaya, E.J.; Karachentsev, I.D.; Makarov, D.I.; Makarova, L.; Wu, P.F.; Dolphin, A.E.; Kourkchi, E. The Extragalactic Distance Database: The Color-Magnitude Diagrams/Tip of the Red Giant Branch Distance Catalog. *AJ* **2021**, *162*, 80, [arXiv:astro-ph.GA/2104.02649]. <https://doi.org/10.3847/1538-3881/ac0440>.
4. Tully, R.B.; Rizzi, L.; Shaya, E.J.; Courtois, H.M.; Makarov, D.I.; Jacobs, B.A. The Extragalactic Distance Database. *AJ* **2009**, *138*, 323–331. <https://doi.org/10.1088/0004-6256/138/2/323>.
5. McCall, M.L. A Council of Giants. *MNRAS* **2014**, *440*, 405–426, [arXiv:astro-ph.GA/1403.3667]. <https://doi.org/10.1093/mnras/stu199>.
6. Smith, S.E.T.; Cerny, W.; Hayes, C.R.; Sestito, F.; Jensen, J.; McConnachie, A.W.; Geha, M.; Navarro, J.F.; Li, T.S.; Cuillandre, J.C.; et al. The Discovery of the Faintest Known Milky Way Satellite Using UNIONS. *ApJ* **2024**, *961*, 92, [arXiv:astro-ph.GA/2311.10147]. <https://doi.org/10.3847/1538-4357/ad0d9f>.
7. Wang, W.; Han, J.; Cautun, M.; Li, Z.; Ishigaki, M.N. The mass of our Milky Way. *Science China Physics, Mechanics, and Astronomy* **2020**, *63*, 109801, [arXiv:astro-ph.GA/1912.02599]. <https://doi.org/10.1007/s11433-019-1541-6>.
8. Bobylev, V.V.; Baykova, A.T. Modern Estimates of the Mass of the Milky Way. *Astronomy Reports* **2023**, *67*, 812–823. <https://doi.org/10.1134/S1063772923080024>.
9. Bhattacharya, S. Weighing Andromeda: Mass estimates of the M<sub>31</sub> galaxy. *arXiv e-prints* **2023**, p. arXiv:2305.03293, [arXiv:astro-ph.GA/2305.03293]. <https://doi.org/10.48550/arXiv.2305.03293>.
10. Karachentsev, I.D.; Kashibadze, O.G.; Makarov, D.I.; Tully, R.B. The Hubble flow around the Local Group. *MNRAS* **2009**, *393*, 1265–1274, [arXiv:astro-ph/0811.4610]. <https://doi.org/10.1111/j.1365-2966.2008.14300.x>.
11. Watkins, L.L.; Evans, N.W.; An, J.H. The masses of the Milky Way and Andromeda galaxies. *MNRAS* **2010**, *406*, 264–278, [arXiv:astro-ph.GA/1002.4565]. <https://doi.org/10.1111/j.1365-2966.2010.16708.x>.

<sup>2</sup> <http://leda.univ-lyon1.fr>

12. Carlesi, E.; Hoffman, Y.; Libeskind, N.I. Estimation of the masses in the local group by gradient boosted decision trees. *MNRAS* **2022**, *513*, 2385–2393, [arXiv:astro-ph.CO/2204.03334]. <https://doi.org/10.1093/mnras/stac897>.
13. Peñarrubia, J.; Ma, Y.Z.; Walker, M.G.; McConnachie, A. A dynamical model of the local cosmic expansion. *MNRAS* **2014**, *443*, 2204–2222, [arXiv:astro-ph.GA/1405.0306]. <https://doi.org/10.1093/mnras/stu879>.
14. Kaisina, E.I.; Makarov, D.I.; Karachentsev, I.D.; Kaisin, S.S. Observational database for studies of nearby universe. *Astrophysical Bulletin* **2012**, *67*, 115–122. <https://doi.org/10.1134/S1990341312010105>.
15. Kashibadze, O.G.; Karachentsev, I.D. Cosmic flow around local massive galaxies. *A&A* **2018**, *609*, A11, [arXiv:astro-ph.CO/1709.09420]. <https://doi.org/10.1051/0004-6361/201731645>.
16. McConnachie, A.W.; Venn, K.A. Revised and New Proper Motions for Confirmed and Candidate Milky Way Dwarf Galaxies. *AJ* **2020**, *160*, 124, [arXiv:astro-ph.GA/2007.05011]. <https://doi.org/10.3847/1538-3881/aba4ab>.
17. Pace, A.B.; Erkal, D.; Li, T.S. Proper Motions, Orbits, and Tidal Influences of Milky Way Dwarf Spheroidal Galaxies. *ApJ* **2022**, *940*, 136, [arXiv:astro-ph.GA/2205.05699]. <https://doi.org/10.3847/1538-4357/ac997b>.
18. Savino, A.; Weisz, D.R.; Skillman, E.D.; Dolphin, A.; Kallivayalil, N.; Wetzel, A.; Anderson, J.; Besla, G.; Boylan-Kolchin, M.; Bullock, J.S.; et al. The Hubble Space Telescope Survey of M31 Satellite Galaxies. I. RR Lyrae-based Distances and Refined 3D Geometric Structure. *ApJ* **2022**, *938*, 101, [arXiv:astro-ph.GA/2206.02801]. <https://doi.org/10.3847/1538-4357/ac91cb>.
19. Drlica-Wagner, A.; Bechtol, K.; Mau, S.; McNanna, M.; Nadler, E.O.; Pace, A.B.; Li, T.S.; Pieres, A.; Rozo, E.; Simon, J.D.; et al. Milky Way Satellite Census. I. The Observational Selection Function for Milky Way Satellites in DES Y3 and Pan-STARRS DR1. *ApJ* **2020**, *893*, 47, [arXiv:astro-ph.GA/1912.03302]. <https://doi.org/10.3847/1538-4357/ab7eb9>.
20. Makarov, D.; Prugniel, P.; Terekhova, N.; Courtois, H.; Vauglin, I. HyperLEDA. III. The catalogue of extragalactic distances. *A&A* **2014**, *570*, A13, [arXiv:astro-ph.GA/1408.3476]. <https://doi.org/10.1051/0004-6361/201423496>.
21. Pawlowski, M.S. Phase-Space Correlations among Systems of Satellite Galaxies. *Galaxies* **2021**, *9*, 66, [arXiv:astro-ph.GA/2109.02654]. <https://doi.org/10.3390/galaxies9030066>.
22. Conn, A.R.; Lewis, G.F.; Ibata, R.A.; Parker, Q.A.; Zucker, D.B.; McConnachie, A.W.; Martin, N.F.; Valls-Gabaud, D.; Tanvir, N.; Irwin, M.J.; et al. The Three-dimensional Structure of the M31 Satellite System; Strong Evidence for an Inhomogeneous Distribution of Satellites. *ApJ* **2013**, *766*, 120, [arXiv:astro-ph.CO/1301.7131]. <https://doi.org/10.1088/0004-637X/766/2/120>.
23. Gaia Collaboration.; Brown, A.G.A.; Vallenari, A.; Prusti, T.; de Bruijne, J.H.J.; Babusiaux, C.; Bailer-Jones, C.A.L.; Biermann, M.; Evans, D.W.; Eyer, L.; et al. Gaia Data Release 2. Summary of the contents and survey properties. *A&A* **2018**, *616*, A1, [arXiv:astro-ph.GA/1804.09365]. <https://doi.org/10.1051/0004-6361/201833051>.
24. Makarov, D.; Khoperskov, S.; Makarov, D.; Makarova, L.; Libeskind, N.; Salomon, J.B. The LMC impact on the kinematics of the Milky Way satellites: clues from the running solar apex. *MNRAS* **2023**, *521*, 3540–3552, [arXiv:astro-ph.GA/2303.06175]. <https://doi.org/10.1093/mnras/stad757>.
25. Akhmetov, V.S.; Bucciarelli, B.; Crosta, M.; Lattanzi, M.G.; Spagna, A.; Re Fiorentin, P.; Bannikova, E.Y. A new kinematic model of the Galaxy: analysis of the stellar velocity field from Gaia Data Release 3. *MNRAS* **2024**, *530*, 710–729, [arXiv:astro-ph.GA/2307.08527]. <https://doi.org/10.1093/mnras/stae772>.
26. Reid, M.J.; Brunthaler, A. The Proper Motion of Sagittarius A\*. III. The Case for a Supermassive Black Hole. *ApJ* **2020**, *892*, 39, [arXiv:astro-ph.GA/2001.04386]. <https://doi.org/10.3847/1538-4357/ab76cd>.
27. GRAVITY Collaboration.; Abuter, R.; Amorim, A.; Bauböck, M.; Berger, J.P.; Bonnet, H.; Brandner, W.; Clénet, Y.; Davies, R.; de Zeeuw, P.T.; et al. Improved GRAVITY astrometric accuracy from modeling optical aberrations. *A&A* **2021**, *647*, A59, [arXiv:astro-ph.GA/2101.12098]. <https://doi.org/10.1051/0004-6361/202040208>.
28. Bajkova, A.T.; Bobylev, V.V. Galactic orbits of selected companions of the Milky Way. *Astronomy Reports* **2017**, *61*, 727–738, [arXiv:astro-ph.GA/1707.04168]. <https://doi.org/10.1134/S1063772917080017>.
29. Boylan-Kolchin, M.; Bullock, J.S.; Sohn, S.T.; Besla, G.; van der Marel, R.P. The Space Motion of Leo I: The Mass of the Milky Way’s Dark Matter Halo. *ApJ* **2013**, *768*, 140, [arXiv:astro-ph.CO/1210.6046]. <https://doi.org/10.1088/0004-637X/768/2/140>.
30. Pacucci, F.; Ni, Y.; Loeb, A. Extreme Tidal Stripping May Explain the Overmassive Black Hole in Leo I: A Proof of Concept. *ApJ* **2023**, *956*, L37, [arXiv:astro-ph.GA/2309.02487]. <https://doi.org/10.3847/2041-8213/acff5e>.

31. van der Marel, R.P.; Fardal, M.A.; Sohn, S.T.; Patel, E.; Besla, G.; del Pino, A.; Sahlmann, J.; Watkins, L.L. First Gaia Dynamics of the Andromeda System: DR2 Proper Motions, Orbits, and Rotation of M31 and M33. *ApJ* **2019**, *872*, 24, [arXiv:astro-ph.GA/1805.04079]. <https://doi.org/10.3847/1538-4357/ab001b>.
32. Salomon, J.B.; Ibata, R.; Reyl , C.; Famaey, B.; Libeskind, N.I.; McConnachie, A.W.; Hoffman, Y. The proper motion of Andromeda from Gaia EDR3: confirming a nearly radial orbit. *MNRAS* **2021**, *507*, 2592–2601, [arXiv:astro-ph.GA/2012.09204]. <https://doi.org/10.1093/mnras/stab2253>.
33. Patel, E.; Mandel, K.S. Evidence for a Massive Andromeda Galaxy Using Satellite Galaxy Proper Motions. *ApJ* **2023**, *948*, 104, [arXiv:astro-ph.GA/2211.15928]. <https://doi.org/10.3847/1538-4357/acc029>.
34. Casetti-Dinescu, D.I.; Pawlowski, M.S.; Girard, T.M.; Kanehisa, K.J.; Petroski, A.; Martone, M.; Kozhurina-Platais, V.; Platais, I. HST Proper Motion of Andromeda III. Another Satellite Coorbiting the M31 Satellite Plane. *ApJ* **2024**, *975*, 138, [arXiv:astro-ph.GA/2409.08252]. <https://doi.org/10.3847/1538-4357/ad7b10>.
35. Collins, M.L.M.; Karim, N.; Martinez-Delgado, D.; Monelli, M.; Tollerud, E.J.; Donatiello, G.; Navabi, M.; Charles, E.; Boschin, W. Pisces VII/Triangulum III - M33's second dwarf satellite galaxy. *MNRAS* **2024**, *528*, 2614–2620, [arXiv:astro-ph.GA/2305.13966]. <https://doi.org/10.1093/mnras/stae199>.
36. Patel, E.; Carlin, J.L.; Tollerud, E.J.; Collins, M.L.M.; Dooley, G.A.  $\Lambda$ CDM predictions for the satellite population of M33. *MNRAS* **2018**, *480*, 1883–1897, [arXiv:astro-ph.GA/1807.05318]. <https://doi.org/10.1093/mnras/sty1946>.
37. Makarova, L.N.; Makarov, D.I.; Karachentsev, I.D.; Tully, R.B.; Rizzi, L. Star formation history of And XVIII: a dwarf spheroidal galaxy in isolation. *MNRAS* **2017**, *464*, 2281–2289, [arXiv:astro-ph.GA/1609.09706]. <https://doi.org/10.1093/mnras/stw2502>.
38. Libeskind, N.I.; Carlesi, E.; Grand, R.J.J.; Khalatyan, A.; Knebe, A.; Pakmor, R.; Pilipenko, S.; Pawlowski, M.S.; Sparre, M.; Tempel, E.; et al. The HESTIA project: simulations of the Local Group. *MNRAS* **2020**, *498*, 2968–2983, [arXiv:astro-ph.GA/2008.04926]. <https://doi.org/10.1093/mnras/staa2541>.
39. Weinberger, R.; Springel, V.; Pakmor, R. The AREPO Public Code Release. *ApJS* **2020**, *248*, 32, [arXiv:astro-ph.IM/1909.04667]. <https://doi.org/10.3847/1538-4365/ab908c>.
40. Tully, R.B.; Courtois, H.M.; Dolphin, A.E.; Fisher, J.R.; H raudeau, P.; Jacobs, B.A.; Karachentsev, I.D.; Makarov, D.; Makarova, L.; Mitronova, S.; et al. Cosmicflows-2: The Data. *AJ* **2013**, *146*, 86, [arXiv:astro-ph.CO/1307.7213]. <https://doi.org/10.1088/0004-6256/146/4/86>.
41. Doumler, T.; Hoffman, Y.; Courtois, H.; Gottl ber, S. Reconstructing cosmological initial conditions from galaxy peculiar velocities - I. Reverse Zeldovich Approximation. *MNRAS* **2013**, *430*, 888–901, [arXiv:astro-ph.CO/1212.2806]. <https://doi.org/10.1093/mnras/sts613>.
42. Grand, R.J.J.; G mez, F.A.; Marinacci, F.; Pakmor, R.; Springel, V.; Campbell, D.J.R.; Frenk, C.S.; Jenkins, A.; White, S.D.M. The Auriga Project: the properties and formation mechanisms of disc galaxies across cosmic time. *MNRAS* **2017**, *467*, 179–207, [arXiv:astro-ph.GA/1610.01159]. <https://doi.org/10.1093/mnras/stx071>.
43. Bland-Hawthorn, J.; Gerhard, O. The Galaxy in Context: Structural, Kinematic, and Integrated Properties. *ARA&A* **2016**, *54*, 529–596, [arXiv:astro-ph.GA/1602.07702]. <https://doi.org/10.1146/annurev-astro-081915-023441>.
44. Drlica-Wagner, A.; Bechtol, K.; Rykoff, E.S.; Luque, E.; Queiroz, A.; Mao, Y.Y.; Wechsler, R.H.; Simon, J.D.; Santiago, B.; Yanny, B.; et al. Eight Ultra-faint Galaxy Candidates Discovered in Year Two of the Dark Energy Survey. *ApJ* **2015**, *813*, 109, [arXiv:astro-ph.GA/1508.03622]. <https://doi.org/10.1088/0004-637X/813/2/109>.
45. Karachentsev, I.D.; Karachentseva, V.E.; Huchtmeier, W.K.; Makarov, D.I. A Catalog of Neighboring Galaxies. *AJ* **2004**, *127*, 2031–2068. <https://doi.org/10.1086/382905>.
46. Walker, M.G.; Mateo, M.; Olszewski, E.W.; Sen, B.; Woodroffe, M. Clean Kinematic Samples in Dwarf Spheroidals: An Algorithm for Evaluating Membership and Estimating Distribution Parameters When Contamination is Present. *AJ* **2009**, *137*, 3109–3138, [arXiv:astro-ph/0811.1990]. <https://doi.org/10.1088/0004-6256/137/2/3109>.
47. Conn, B.C.; Jerjen, H.; Kim, D.; Schirmer, M. On the Nature of Ultra-faint Dwarf Galaxy Candidates. I. DES1, Eridanus III, and Tucana V. *ApJ* **2018**, *852*, 68, [arXiv:astro-ph.GA/1712.01439]. <https://doi.org/10.3847/1538-4357/aa9eda>.
48. Cerny, W.; Pace, A.B.; Drlica-Wagner, A.; Ferguson, P.S.; Mau, S.; Adam w, M.; Carlin, J.L.; Choi, Y.; Erkal, D.; Johnson, L.C.; et al. Discovery of an Ultra-faint Stellar System near the Magellanic Clouds with the DECam Local Volume Exploration Survey. *ApJ* **2021**, *910*, 18, [arXiv:astro-ph.GA/2009.08550]. <https://doi.org/10.3847/1538-4357/abe1af>.

49. Carlin, J.L.; Sand, D.J.; Muñoz, R.R.; Spekkens, K.; Willman, B.; Crnojević, D.; Forbes, D.A.; Hargis, J.; Kirby, E.; Peter, A.H.G.; et al. Deep Subaru Hyper Suprime-Cam Observations of Milky Way Satellites Columba I and Triangulum II. *AJ* **2017**, *154*, 267, [arXiv:astro-ph.GA/1710.06444]. <https://doi.org/10.3847/1538-3881/aa94d0>.
50. Luque, E.; Pieres, A.; Santiago, B.; Yanny, B.; Vivas, A.K.; Queiroz, A.; Drlica-Wagner, A.; Morganson, E.; Balbinot, E.; Marshall, J.L.; et al. The Dark Energy Survey view of the Sagittarius stream: discovery of two faint stellar system candidates. *MNRAS* **2017**, *468*, 97–108, [arXiv:astro-ph.GA/1608.04033]. <https://doi.org/10.1093/mnras/stx405>.
51. Ferrarese, L.; Mould, J.R.; Kennicutt, Jr., R.C.; Huchra, J.; Ford, H.C.; Freedman, W.L.; Stetson, P.B.; Madore, B.F.; Sakai, S.; Gibson, B.K.; et al. The Hubble Space Telescope Key Project on the Extragalactic Distance Scale. XXVI. The Calibration of Population II Secondary Distance Indicators and the Value of the Hubble Constant. *ApJ* **2000**, *529*, 745–767, [arXiv:astro-ph/9908192]. <https://doi.org/10.1086/308309>.
52. Strauss, M.A.; Huchra, J.P.; Davis, M.; Yahil, A.; Fisher, K.B.; Tonry, J. A Redshift Survey of IRAS Galaxies. VII. The Infrared and Redshift Data for the 1.936 Jansky Sample. *ApJS* **1992**, *83*, 29. <https://doi.org/10.1086/191730>.
53. Hargis, J.R.; Kimmig, B.; Willman, B.; Caldwell, N.; Walker, M.G.; Strader, J.; Sand, D.J.; Grillmair, C.J.; Yoon, J.H. Evidence That Hydra I is a Tidally Disrupting Milky Way Dwarf Galaxy. *ApJ* **2016**, *818*, 39, [arXiv:astro-ph.GA/1509.06391]. <https://doi.org/10.3847/0004-637X/818/1/39>.
54. Torrealba, G.; Belokurov, V.; Koposov, S.E.; Li, T.S.; Walker, M.G.; Sanders, J.L.; Geringer-Sameth, A.; Zucker, D.B.; Kuehn, K.; Evans, N.W.; et al. The hidden giant: discovery of an enormous Galactic dwarf satellite in Gaia DR2. *MNRAS* **2019**, *488*, 2743–2766, [arXiv:astro-ph.GA/1811.04082]. <https://doi.org/10.1093/mnras/stz1624>.
55. Ji, A.P.; Koposov, S.E.; Li, T.S.; Erkal, D.; Pace, A.B.; Simon, J.D.; Belokurov, V.; Cullinane, L.R.; Da Costa, G.S.; Kuehn, K.; et al. Kinematics of Antlia 2 and Crater 2 from the Southern Stellar Stream Spectroscopic Survey (S<sup>5</sup>). *ApJ* **2021**, *921*, 32, [arXiv:astro-ph.GA/2106.12656]. <https://doi.org/10.3847/1538-4357/ac1869>.
56. McQuinn, K.B.W.; Mao, Y.Y.; Tollerud, E.J.; Cohen, R.E.; Shih, D.; Buckley, M.R.; Dolphin, A.E. Discovery and Characterization of Two Ultrafaint Dwarfs outside the Halo of the Milky Way: Leo M and Leo K. *ApJ* **2024**, *967*, 161, [arXiv:astro-ph.GA/2307.08738]. <https://doi.org/10.3847/1538-4357/ad429b>.
57. Laevens, B.P.M.; Martin, N.F.; Sesar, B.; Bernard, E.J.; Rix, H.W.; Slater, C.T.; Bell, E.F.; Ferguson, A.M.N.; Schlafly, E.F.; Burgett, W.S.; et al. A New Distant Milky Way Globular Cluster in the Pan-STARRS1  $3\pi$  Survey. *ApJ* **2014**, *786*, L3, [arXiv:astro-ph.GA/1403.6593]. <https://doi.org/10.1088/2041-8205/786/1/L3>.
58. Kirby, E.N.; Simon, J.D.; Cohen, J.G. Spectroscopic Confirmation of the Dwarf Galaxies Hydra II and Pisces II and the Globular Cluster Laevens 1. *ApJ* **2015**, *810*, 56, [arXiv:astro-ph.GA/1506.01021]. <https://doi.org/10.1088/0004-637X/810/1/56>.
59. Mau, S.; Cerny, W.; Pace, A.B.; Choi, Y.; Drlica-Wagner, A.; Santana-Silva, L.; Riley, A.H.; Erkal, D.; Stringfellow, G.S.; Adamów, M.; et al. Two Ultra-faint Milky Way Stellar Systems Discovered in Early Data from the DECam Local Volume Exploration Survey. *ApJ* **2020**, *890*, 136, [arXiv:astro-ph.GA/1912.03301]. <https://doi.org/10.3847/1538-4357/ab6c67>.
60. Simon, J.D.; Geha, M. The Kinematics of the Ultra-faint Milky Way Satellites: Solving the Missing Satellite Problem. *ApJ* **2007**, *670*, 313–331, [arXiv:astro-ph/0706.0516]. <https://doi.org/10.1086/521816>.
61. Grillmair, C.J. Four New Stellar Debris Streams in the Galactic Halo. *ApJ* **2009**, *693*, 1118–1127, [arXiv:astro-ph/0811.3965]. <https://doi.org/10.1088/0004-637X/693/2/1118>.
62. Gregory, A.L.; Collins, M.L.M.; Erkal, D.; Tollerud, E.; Delorme, M.; Hill, L.; Sand, D.J.; Strader, J.; Willman, B. Uncovering the orbit of the hercules dwarf galaxy. *MNRAS* **2020**, *496*, 1092–1104, [arXiv:astro-ph.GA/1912.00156]. <https://doi.org/10.1093/mnras/staa1553>.
63. GRAVITY Collaboration.; Abuter, R.; Amorim, A.; Anugu, N.; Bauböck, M.; Benisty, M.; Berger, J.P.; Blind, N.; Bonnet, H.; Brandner, W.; et al. Detection of the gravitational redshift in the orbit of the star S2 near the Galactic centre massive black hole. *A&A* **2018**, *615*, L15, [arXiv:astro-ph.GA/1807.09409]. <https://doi.org/10.1051/0004-6361/201833718>.
64. Monaco, L.; Bellazzini, M.; Ferraro, F.R.; Pancino, E. The distance to the Sagittarius dwarf spheroidal galaxy from the red giant branch tip. *MNRAS* **2004**, *353*, 874–878, [arXiv:astro-ph/0406350]. <https://doi.org/10.1111/j.1365-2966.2004.08122.x>.
65. Kirby, E.N.; Bullock, J.S.; Boylan-Kolchin, M.; Kaplinghat, M.; Cohen, J.G. The dynamics of isolated Local Group galaxies. *MNRAS* **2014**, *439*, 1015–1027, [arXiv:astro-ph.GA/1401.1208]. <https://doi.org/10.1093/mnras/stu025>.

66. Longeard, N.; Martin, N.; Ibata, R.A.; Starkenburg, E.; Jablonka, P.; Aguado, D.S.; Carlberg, R.G.; Côté, P.; González Hernández, J.I.; Lucchesi, R.; et al. The pristine dwarf-galaxy survey - III. Revealing the nature of the Milky Way globular cluster Sagittarius II. *MNRAS* **2021**, *503*, 2754–2762, [arXiv:astro-ph.GA/2005.05976]. <https://doi.org/10.1093/mnras/stab604>.
67. Fadely, R.; Willman, B.; Geha, M.; Walsh, S.; Muñoz, R.R.; Jerjen, H.; Vargas, L.C.; Da Costa, G.S. Segue 3: An Old, Extremely Low Luminosity Star Cluster in the Milky Way's Halo. *AJ* **2011**, *142*, 88, [arXiv:astro-ph.GA/1107.3151]. <https://doi.org/10.1088/0004-6256/142/3/88>.
68. Fritz, T.K.; Carrera, R.; Battaglia, G.; Taibi, S. Gaia DR 2 and VLT/FLAMES search for new satellites of the LMC. *A&A* **2019**, *623*, A129, [arXiv:astro-ph.GA/1805.07350]. <https://doi.org/10.1051/0004-6361/201833458>.
69. Huxor, A.P.; Mackey, A.D.; Ferguson, A.M.N.; Irwin, M.J.; Martin, N.F.; Tanvir, N.R.; Veljanoski, J.; McConnachie, A.; Fishlock, C.K.; Ibata, R.; et al. The outer halo globular cluster system of M31 - I. The final PAndAS catalogue. *MNRAS* **2014**, *442*, 2165–2187, [arXiv:astro-ph.GA/1404.5807]. <https://doi.org/10.1093/mnras/stu771>.
70. Weisz, D.R.; Dolphin, A.E.; Martin, N.F.; Albers, S.M.; Collins, M.L.M.; Ferguson, A.M.N.; Lewis, G.F.; Mackey, A.D.; McConnachie, A.; Rich, R.M.; et al. A rogues gallery of Andromeda's dwarf galaxies - II. Precise distances to 17 faint satellites. *MNRAS* **2019**, *489*, 763–770, [arXiv:astro-ph.GA/1909.02017]. <https://doi.org/10.1093/mnras/stz1984>.
71. Watkins, L.L.; Evans, N.W.; van de Ven, G. A census of orbital properties of the M31 satellites. *MNRAS* **2013**, *430*, 971–985, [arXiv:astro-ph.CO/1211.2638]. <https://doi.org/10.1093/mnras/sts634>.
72. Karachentsev, I.D.; Kaisina, E.I.; Makarov, D.I. Suites of Dwarfs around nearby Giant Galaxies. *AJ* **2014**, *147*, 13, [arXiv:astro-ph.CO/1310.6838]. <https://doi.org/10.1088/0004-6256/147/1/13>.
73. Oh, S.H.; Hunter, D.A.; Brinks, E.; Elmegreen, B.G.; Schruha, A.; Walter, F.; Rupen, M.P.; Young, L.M.; Simpson, C.E.; Johnson, M.C.; et al. High-resolution Mass Models of Dwarf Galaxies from LITTLE THINGS. *AJ* **2015**, *149*, 180, [arXiv:astro-ph.GA/1502.01281]. <https://doi.org/10.1088/0004-6256/149/6/180>.
74. Martin, N.F.; Chambers, K.C.; Collins, M.L.M.; Ibata, R.A.; Rich, R.M.; Bell, E.F.; Bernard, E.J.; Ferguson, A.M.N.; Flewelling, H.; Kaiser, N.; et al. Spectroscopy of the Three Distant Andromedan Satellites Cassiopeia III, Lacerta I, and Perseus I. *ApJ* **2014**, *793*, L14, [arXiv:astro-ph.GA/1408.5130]. <https://doi.org/10.1088/2041-8205/793/1/L14>.
75. Richardson, J.C.; Irwin, M.J.; McConnachie, A.W.; Martin, N.F.; Dotter, A.L.; Ferguson, A.M.N.; Ibata, R.A.; Chapman, S.C.; Lewis, G.F.; Tanvir, N.R.; et al. PAndAS' Progeny: Extending the M31 Dwarf Galaxy Cabal. *ApJ* **2011**, *732*, 76, [arXiv:astro-ph.CO/1102.2902]. <https://doi.org/10.1088/0004-637X/732/2/76>.
76. Martin, N.F.; Ibata, R.A.; Irwin, M.J.; Chapman, S.; Lewis, G.F.; Ferguson, A.M.N.; Tanvir, N.; McConnachie, A.W. Discovery and analysis of three faint dwarf galaxies and a globular cluster in the outer halo of the Andromeda galaxy. *MNRAS* **2006**, *371*, 1983–1991, [arXiv:astro-ph/0607472]. <https://doi.org/10.1111/j.1365-2966.2006.10823.x>.
77. Sakari, C.M.; Wallerstein, G. The integrated calcium II triplet as a metallicity indicator: comparisons with high-resolution [Fe/H] in M31 globular clusters. *MNRAS* **2016**, *456*, 831–843, [arXiv:astro-ph.GA/1511.06766]. <https://doi.org/10.1093/mnras/stv2711>.
78. Mackey, A.D.; Huxor, A.P.; Martin, N.F.; Ferguson, A.M.N.; Dotter, A.; McConnachie, A.W.; Ibata, R.A.; Irwin, M.J.; Lewis, G.F.; Sakari, C.M.; et al. A Peculiar Faint Satellite in the Remote Outer Halo of M31. *ApJ* **2013**, *770*, L17, [arXiv:astro-ph.GA/1304.7826]. <https://doi.org/10.1088/2041-8205/770/2/L17>.
79. Collins, M.L.M.; Chapman, S.C.; Rich, R.M.; Ibata, R.A.; Martin, N.F.; Irwin, M.J.; Bate, N.F.; Lewis, G.F.; Peñarrubia, J.; Arimoto, N.; et al. A Kinematic Study of the Andromeda Dwarf Spheroidal System. *ApJ* **2013**, *768*, 172, [arXiv:astro-ph.CO/1302.6590]. <https://doi.org/10.1088/0004-637X/768/2/172>.
80. Alam, S.; Albareti, F.D.; Allende Prieto, C.; Anders, F.; Anderson, S.F.; Anderton, T.; Andrews, B.H.; Armengaud, E.; Aubourg, É.; Bailey, S.; et al. The Eleventh and Twelfth Data Releases of the Sloan Digital Sky Survey: Final Data from SDSS-III. *ApJS* **2015**, *219*, 12, [arXiv:astro-ph.IM/1501.00963]. <https://doi.org/10.1088/0067-0049/219/1/12>.

## Appendix A List of satellites of the Milky Way

**Table A1.** Known satellites of the Milky Way galaxy.

Name	J2000	$(m - M)_0$	Method	$D$		$V_h$	
		mag		kpc		km s <sup>-1</sup>	
Tucana IV	000255.2–605100	18.41 ±0.19 [44]	TRGB	48.1	±4.4	15.9	<sup>+1.8</sup> <sub>-1.7</sub> [16]
SMC	005238.0–724801	18.99 ±0.05 [16]	Cep	62.8	±1.5	158	±4 [45]
Sculptor	010009.4–334233	19.67 ±0.14 [16]	TRGB	85.9	±5.7	111.4	±0.1 [46]
Cetus II	011752.8–172512	17.10 ±0.10 [47]	CMD	26.3	±1.2		
DELVE 2	015505.3–681511	19.26 ±0.10 [48]	HB	71.1	±3.4		
Cetus III	020519.4–041612	22.00 <sup>+0.20</sup> <sub>-0.10</sub> [16]	HB	251	<sup>+24</sup> <sub>-12</sub>		
Triangulum II	021317.4+361042	17.27 ±0.11 [49]	CMD	28.4	±1.5	-381.70	±1.10 [16]
Segue 2	021916.0+201031	17.70 ±0.10 [16]	TRGB	34.7	±1.6	-40.20	±0.90 [17]
Eridanus III	022245.5–521701	19.70 ±0.15 [16]	HB	87.1	±6.2		
DES J0225+0304	022542.4+030410	16.88 <sup>+0.06</sup> <sub>-0.05</sub> [50]	CMD	23.8	<sup>+0.7</sup> <sub>-0.6</sub>		
Hydrus I	022933.4–784128	17.20 ±0.04 [16]	TRGB	27.5	±0.5	80.4	±0.6 [16]
Fornax	023954.7–343133	20.84 ±0.18 [16]	TRGB	147	±13	55.2	±0.1 [46]
Horologium I	025531.7–540708	19.50 ±0.20 [16]	HB	79.4	±7.7	112.8	<sup>+2.5</sup> <sub>-2.6</sub> [16]
Horologium II	031632.1–500105	19.46 ±0.20 [16]	HB	78.0	±7.5	168.7	<sup>+12.9</sup> <sub>-12.6</sub> [16]
Reticulum II	033542.1–540257	17.40 ±0.15 [16]	HB	30.2	±2.2	64.7	<sup>+1.3</sup> <sub>-0.8</sub> [16]
Reticulum III	034526.4–602700	19.81 ±0.31 [16]	CMD	92	±14	274.2	<sup>+7.5</sup> <sub>-7.4</sub> [16]
Pictor I	044347.4–501659	20.30 ±0.15 [16]	HB	115	±8		
LMC	052334.6–694522	18.50 ±0.13 [51]	Cep	50.1	±3.1	278	±2 [52]
Columba I	053125.7–275727	21.31 ±0.11 [49]	BHB	183	±10	153.7	<sup>+5</sup> <sub>-4.8</sub> [16]
Carina	064136.7–505758	20.11 ±0.13 [16]	TRGB	105	±7	222.9	±0.1 [16]
Pictor II	064443.2–595360	18.30 <sup>+0.12</sup> <sub>-0.15</sub> [16]	HB	45.7	<sup>+2.6</sup> <sub>-3.3</sub>		
Carina II	073625.6–560003	17.79 ±0.05 [16]	HB	36.1	±0.8	477.2	±1.2 [16]
Carina III	073831.2–560601	17.22 ±0.10 [16]	HB	27.8	±1.3	284.6	<sup>+3.4</sup> <sub>-3.1</sub> [16]
Ursa Major II	085130.0+630748	17.50 ±0.30 [16]	TRGB	31.6	±4.7	-116.5	±1.9 [16]
HYDRA 1	085536.0+033600	15.52 ±0.05 [53]	MS	12.7	±0.3	89	±1.4 [53]
Antlia II	093532.8–364602	20.6 ±0.11 [54]	HBH	132	±7	288.8	±0.4 [55]
Segue 1	100703.2+160425	16.8 ±0.20 [16]	CMD	22.9	±2.2	208.5	±0.9 [16]
Leo I	100826.9+121829	22.02 ±0.13 [16]	TRGB	254	±16	282.5	±0.1 [16]
Sextans dSph	101303.0–013652	19.67 ±0.10 [16]	TRGB	85.9	±4.0	224.2	±0.1 [16]
Sextans II	102544.9–003752	20.50 ±0.20 [56]	HB	126	±12		
Ursa Major I	103448.8+515606	19.93 ±0.10 [16]	TRGB	97	±5	-55.3	±1.4 [16]
Willman 1	104921.0+510260	17.90 ±0.40 [16]	CMD	38.0	±7.7	-12.8	±1 [17]
Leo II	111329.2+220917	21.84 ±0.13 [16]	TRGB	233	±14	78	±0.1 [16]
Leo V	113109.6+021312	21.46 ±0.16 [16]	TRGB	196	±15	170.9	<sup>+2.1</sup> <sub>-1.9</sub> [16]
Leo IV	113257.0+003160	20.94 ±0.09 [16]	HB	154	±7	132.3	±1.4 [16]
Crater	113615.8–105240	20.81 ±0.12 [57]	HB	145	±8	149.3	±1.2 [58]
Crater II	114914.4–182447	20.35 ±0.02 [16]	TRGB	118	±1	89.3	±0.3 [55]
Virgo I	120009.6+004048	19.80 ±0.20 [16]	HB	91	±9		
Hydra II	122142.1–315907	20.64 ±0.16 [16]	TRGB	134	±10	303.1	±1.4 [16]
Coma Berenices	122658.4+235442	18.13 ±0.08 [16]	HB	42.3	±1.6	98.1	±0.9 [16]
Centaurus I	123820.4–405407	20.33 ±0.10 [59]	HB	116	±6		
Canes Venatici II	125710.0+341915	21.02 ±0.06 [16]	HB	160	±5	-129	±1.2 [16]
Canes Venatici I	132803.5+333321	21.69 ±0.10 [16]	TRGB	218	±10	30.9	±0.6 [60]
Bootes III	135712.0+264800	18.35 ±0.10 [61]	HB	46.8	±2.2	197.5	±3.8 [14]
Bootes II	135808.0+125054	18.10 ±0.06 [16]	TRGB	41.7	±1.2	-117	±5.2 [16]
Bootes I	140005.0+143015	19.11 ±0.08 [16]	HB	66.4	±2.5	101.8	±0.7 [17]
Ursa Minor	150911.3+671252	19.40 ±0.10 [16]	TRGB	75.9	±3.6	-246.9	±0.1 [16]
Bootes IV	153445.4+434334	21.60 ±0.20 [16]	HB	209	±20		
Draco II	155247.6+643355	16.67 ±0.05 [16]	TRGB	21.6	±0.5	342.5	<sup>+1.1</sup> <sub>-1.2</sub> [16]
DELVE 1	163054.0+005819	16.39 ±0.10 [59]	HB	19.0	±0.9		
Hercules	163103.6+124724	20.84 ±0.20 [16]	TRGB	147	±14	46.4	±1.3 [62]
Draco	172001.4+575434	19.40 ±0.17 [16]	TRGB	76	±6	-291	±0.1 [16]
<b>Milky Way</b>	174540.0–290028	14.55 ±0.01 [63]	Direct	8.1	±0.0	-9.5	±0.0 [25]
Sagittarius dSph	185503.1–302842	17.10 ±0.15 [64]	TRGB	26.3	±1.9	140	±2 [65]
Sagittarius II	195240.5–220405	19.32 <sup>+0.03</sup> <sub>-0.02</sub> [16]	CMD	73.1	<sup>+1.0</sup> <sub>-0.7</sub>	-177.2	<sup>+0.5</sup> <sub>-0.6</sub> [66]
Indus II	203852.8–460936	21.65 ±0.16 [16]	CMD	214	±16		
Indus I	210850.0–510949	20.00 ±0.20 [16]	HB	100	±10		

Name	J2000	$(m - M)_0$	Method	$D$		$V_h$	
		mag		kpc	km s <sup>-1</sup>		
Segue 3	212131.0+190702	16.16 ± 0.09 [67]	CMD	17.1 ± 0.7	-167.1 ± 1.5 [67]		
Grus II	220404.8-462624	18.62 ± 0.21 [16]	CMD	53 ± 5	-110 ± 0.5 [16]		
Pegasus III	222422.6+052512	21.56 ± 0.20 [16]	CMD	205 ± 20	-222.9 ± 2.6 [16]		
Aquarius II	223355.5-091939	20.16 ± 0.07 [16]	TRGB	108 ± 4	-71.1 ± 2.5 [16]		
Tucana II	225155.1-583408	18.80 ± 0.20 [16]	HB	58 ± 6	-129.1 ± 3.5 [16]		
Grus I	225642.4-500948	20.40 ± 0.20 [16]	TRGB	120 ± 12	-140.5 ± 2.4 ± 1.6 [16]		
Pisces II	225831.0+055709	21.31 ± 0.17 [16]	TRGB	183 ± 15	-226.5 ± 2.7 [16]		
Tucana V	233724.0-631612	18.71 ± 0.34 [16]	CMD	55 ± 9	-36.2 ± 2.5 ± 2.2 [16]		
Phoenix II	233959.4-542422	19.60 ± 0.15 [16]	HB	83 ± 6	32.4 ± 3.7 ± 3.8 [68]		
Tucana III	235636.0-593600	17.01 ± 0.16 [16]	TRGB	25.2 ± 1.9	-102.3 ± 0.4 [17]		

**Notes.** The columns contain: (1) galaxy name; (2) J2000 equatorial coordinates; (3–5)  $(m - M)_0$  — distance modulus and its source; (6) distance determination method; (7–8)  $D$  — radial distance in kpc; (9–11)  $V_h$  — heliocentric line-of-sight velocity in km s<sup>-1</sup> and its source.

## Appendix B List of satellites of the Andromeda Galaxy

**Table A2.** Known satellites of the Andromeda Galaxy.

Name	Alt Name	J2000	$(m - M)_0$	Method	$D$		$V_h$	
			mag		kpc	km s <sup>-1</sup>		
PAndAS-05		000024.1+435535				-183.0 ± 7.0 [69]		
And XVIII		000214.5+450520	25.43 <sup>+0.05</sup> <sub>-0.03</sub> [70]	HB	1219 <sup>+28</sup> <sub>-17</sub>	-332.1 ± 2.7 [71]		
PAndAS-04		000442.9+472142				-397.0 ± 7.0 [69]		
And XX		000730.7+350756	24.35 ± 0.08 [18]	RR Lyr	741 ± 28	-456.2 <sup>+3.0</sup> <sub>-3.4</sub> [71]		
IC 10		002024.5+591730	24.50 ± 0.12 [72]	TRGB	794 ± 45	-348.0 ± 2.9 [73]		
And XXVI		002345.6+475558	24.48 <sup>+0.06</sup> <sub>-0.07</sub> [18]	RR Lyr	787 <sup>+22</sup> <sub>-26</sub>	-260.6 <sup>+4.0</sup> <sub>-3.7</sub> [71]		
And XXV		003008.9+465107	24.38 <sup>+0.07</sup> <sub>-0.06</sub> [18]	RR Lyr	752 <sup>+25</sup> <sub>-21</sub>	-107.8 <sup>+1.0</sup> <sub>-0.9</sub> [71]		
NGC 147		003350.8+483028	24.33 ± 0.06 [18]	RR Lyr	735 ± 21	-193.0 ± 3.0 [71]		
And III		003533.8+362952	24.29 ± 0.05 [18]	RR Lyr	721 ± 17	-344.3 ± 1.7 [71]		
Cas III	And XXXII	003559.4+513335	24.52 ± 0.06 [18]	RR Lyr	802 ± 22	-371.6 ± 0.7 [74]		
And XXX		003634.9+493848	23.74 ± 0.06 [18]	RR Lyr	560 ± 16	-141.4 <sup>+5.8</sup> <sub>-6.7</sub> [71]		
And XVII		003707.0+441920	24.40 ± 0.07 [18]	RR Lyr	759 ± 25	-251.1 <sup>+1.5</sup> <sub>-1.6</sub> [71]		
And XXVII		003727.1+452313	24.59 ± 0.12 [75]	HB	828 ± 47	-534.8 <sup>+5.4</sup> <sub>-4.9</sub> [71]		
NGC 185		003858.0+482010	24.06 ± 0.06 [18]	RR Lyr	649 ± 18	-202.0 ± 3.0 [71]		
NGC 205		004022.5+414111	24.61 ± 0.06 [18]	RR Lyr	836 ± 23	-241.0 ± 3.0 [71]		
M 32		004242.1+405259	24.44 ± 0.06 [18]	RR Lyr	773 ± 22	-200.0 ± 6.0 [71]		
<b>M 31</b>		004244.5+411609	24.45 ± 0.06 [18]	RR Lyr	776 ± 22	-301.0 ± 1.0 [71]		
And I		004540.0+380214	24.45 ± 0.05 [18]	RR Lyr	776 ± 18	-376.3 ± 2.2 [71]		
And XI		004620.0+334805	24.38 ± 0.07 [18]	RR Lyr	752 ± 25	-427.0 <sup>+2.9</sup> <sub>-2.8</sub> [71]		
And XII		004727.0+342229	24.28 <sup>+0.08</sup> <sub>-0.07</sub> [18]	RR Lyr	718 <sup>+27</sup> <sub>-24</sub>	-557.1 ± 1.7 [71]		
Bol 520		005042.4+325559	24.00 ± 0.20 [76]	TRGB	631 ± 61	-370.0 ± 5.0 [77]		
And XIV		005135.0+294149	24.44 ± 0.06 [18]	RR Lyr	773 ± 22	-480.6 ± 1.2 [71]		
And XIII		005151.0+330016	24.57 ± 0.07 [18]	RR Lyr	820 ± 27	-185.4 ± 2.4 [71]		
And IX		005252.8+431200	24.60 ± 0.06 [18]	RR Lyr	832 ± 23	-209.4 ± 2.5 [71]		
PAndAS-48		005928.2+312910	24.57 ± 0.11 [78]	HB	820 ± 43	-250.0 ± 5.0 [69]		
And XVI		005929.8+322236	23.57 ± 0.08 [18]	RR Lyr	518 ± 19	-367.3 ± 2.8 [71]		
PAndAS-50		010150.6+481819				-323.0 ± 7.0 [69]		
LGS 3	Pisces I	010355.0+215306	23.91 ± 0.05 [18]	RR Lyr	605 ± 14	-286.5 ± 0.3 [71]		
And X		010633.7+444816	24.00 ± 0.06 [18]	RR Lyr	631 ± 18	-164.1 ± 1.7 [71]		
And V		011017.1+473741	24.58 ± 0.06 [18]	RR Lyr	824 ± 23	-397.4 ± 1.5 [71]		
And XV		011418.7+380703	24.37 ± 0.05 [18]	RR Lyr	748 ± 17	-323.0 ± 1.4 [71]		
And II		011629.8+332509	24.12 ± 0.05 [18]	RR Lyr	667 <sup>+16</sup> <sub>-16</sub>	-193.6 ± 1.0 [71]		
And XXIV		011830.0+462258	23.92 ± 0.07 [18]	RR Lyr	608 ± 20	-127.8 <sup>+5.3</sup> <sub>-5.4</sub> [71]		
And XXIX		011830.0+304520	24.26 ± 0.06 [18]	RR Lyr	711 ± 20	-194.4 ± 1.5 [79]		
Tri III	Pisces VII	012141.3+262332	24.81 <sup>+0.15</sup> <sub>-0.13</sub> [78]	TRGB	916 <sup>+65</sup> <sub>-53</sub>	-138.6 ± 0.5 [80]		
PAndAS-56		012303.5+415511				-239.0 ± 8.0 [69]		
And XXII		012740.0+280525	24.39 ± 0.07 [18]	RR Lyr	755 ± 25	-129.0 <sup>+2.1</sup> <sub>-2.2</sub> [71]		
PAndAS-57		012747.5+404047				-186.0 ± 6.0 [69]		
PAndAS-58		012902.1+404708				-167.0 ± 10.0 [69]		

Name	Alt Name	J2000	$(m - M)_0$ mag	Method	$D$ kpc	$V_h$ km s <sup>-1</sup>
And XXIII		012921.8+384308	24.36 ± 0.07 [18]	RR Lyr	745 ± 24	-242.7 ± 1.0 [71]
M 33		013350.8+303937	24.67 ± 0.06 [18]	RR Lyr	859 ± 24	-180.0 ± 1.0 [71]
Per I	And XXXIII	030123.6+405918	24.24 ± 0.06 [18]	RR Lyr	705 ± 20	-325.9 ± 3.0 [74]
And XXVIII		223241.2+311358	24.36 ± 0.05 [18]	RR Lyr	745 ± 17	-326.2 ± 2.7 [79]
Lac I	And XXXI	225816.3+411728	24.36 ± 0.05 [18]	RR Lyr	745 ± 17	-198.4 ± 1.1 [74]
Cas dSph	And VII	232631.8+504032	24.40 ± 0.06 [18]	RR Lyr	759 ± 21	-307.2 ± 1.3 [71]
Pegasus	Peg DIG	232827.6+144434	24.74 ± 0.05 [18]	RR Lyr	887 ± 21	-184.5 ± 0.3 [71]
Peg dSph	And VI	235146.9+243557	24.23 ± 0.06 [18]	RR Lyr	702 ± 20	-340.8 ± 1.9 [71]
And XXI		235447.7+422815	24.44 $^{+0.06}_{-0.07}$ [18]	RR Lyr	773 $^{+22}_{-25}$	-362.7 ± 0.8 [71]
PAndAS-01		235712.0+433308				-333.0 ± 21.0 [69]
PAndAS-02		235755.6+414649				-226.0 ± 4.0 [69]
And XIX		235855.6+350237	24.55 $^{+0.09}_{-0.08}$ [18]	RR Lyr	813 $^{+34}_{-31}$	-111.2 $^{+1.2}_{-1.3}$ [71]

**Notes.** The columns contain: (1) galaxy name; (2) alternative name; (3) J2000 equatorial coordinates; (4–6)  $(m - M)_0$  — distance modulus and its source; (7) method for distance modulus; (8–9)  $D$  – radial distance in kpc; (10–12)  $V_h$  – heliocentric line-of-sight velocity in km/s and its source.